Remote Sensing of Environment 318 (2025) 114561

Contents lists available at ScienceDirect

Remote Sensing of Environment

journal homepage: www.elsevier.com/locate/rse

Unveiling multimodal consolidation process of the newly reclaimed HKIA 3rd runway from satellite SAR interferometry, ICA analytics and Terzaghi consolidation theory

Zhuo Jiang [a,e], Guoqiang Shi [a,b,c,*], Songbo Wu [a,b,c], Xiaoli Ding [a,b], Chaoying Zhao [e], Man Sing Wong [a,b,d], Zhong Lu [f]

[a] Department of Land Surveying and Geo-Informatics, The Hong Kong Polytechnic University, Kowloon, Hong Kong, China
[b] Research Institute for Land and Space, The Hong Kong Polytechnic University, Hong Kong, China
[c] Shenzhen Research Institute, The Hong Kong Polytechnic University, Shenzhen, China
[d] Research Institute for Sustainable Urban Development, The Hong Kong Polytechnic University, Hong Kong, China
[e] School of Geological Engineering and Geomatics, Chang'an University, Xi'an, China
[f] The Roy M. Huffington Department of Earth Sciences, South Methodist University, Dallas, TX 75275, USA.

ARTICLE INFO

Edited by Jing M. Chen

Keywords:
MTInSAR
New reclamations
Consolidation theory
ICA
HKIA

ABSTRACT

The three-runway system expansion project of the Hong Kong International Airport (HKIA) began with the land reclamation to the north of its original runway. To facilitate quick stabilization, the Deep Cement Mixing (DCM) in this project was featured as the novel reclamation method firstly applied in Hong Kong. Understanding ground deformation and underground consolidation is crucial for subsequent soil improvement, civil construction, and future planning at the new platform. Synthetic Aperture Radar Interferometry (InSAR) is used to investigate the spatiotemporal characteristics of land deformation following the completion of the third runway pavement. A combined strategy of persistent scatterer (PS) and distributed scatterer (DS) interferometry was implemented to address low radar coherence at the site. The new reclamation is subject to varying degrees of land subsidence, with a maximum monitored sinking rate to be ~150 mm/year during September 2021 and October 2023. Whereas the 3rd runway was urgently transformed to operation, spatial details of consolidation status of this new land were not yet evaluated. We applied the Independent Component Analysis (ICA) to identify the underlying sources leading to the measured deformation from InSAR. Three distinct sources have been unveiled, including an exponential decay signal (a quick compaction subsidence of surficial materials), a linear signal (a continuous subsiding from marine deposits) and a periodic signal (thermal effects correlated with buildings and bridges). Notably, the linear deformation component is mainly located in areas with prefabricated vertical drains (PVD), which is strongly correlating with the current monitored subsidence pattern. We incorporated the Terzaghi consolidation theory to further characterize InSAR displacement and estimate the subsidence decay property, consolidation time, ultimate primary settlement and consolidation degree at the 3rd runway, with unprecedented spatial details. Our results indicate the DCM method achieves geological stability more rapidly than the PVD method, with a time advantage of approximately 0.08–1.39 years. Meanwhile, DCM can effectively control the primary settlement to 29 % - 83 % of the PVD method. This research benefits our understanding of the consolidation process at the 3rd runway and offer reliable and detailed data of underground properties. This facilitates more accurate planning of follow-up reinforcement measures at specific locations if needed, which also serves as a valuable reference for future reclamation practices in Hong Kong, particularly using the DCM method.

1. Introduction

Land reclamation is a widely adopted strategy for creating usable land to accommodate growing spatial demands and support future development around the world (Mario Martín-Antón et al., 2016). In Hong Kong, it appears to be the preferred urban development approach

* Corresponding author at: Department of Land Surveying and Geo-Informatics, The Hong Kong Polytechnic University, Kowloon, Hong Kong, China.
E-mail address: guoqiang.shi@polyu.edu.hk (G. Shi).

https://doi.org/10.1016/j.rse.2024.114561
Received 5 June 2024; Received in revised form 20 November 2024; Accepted 3 December 2024
Available online 17 December 2024

to address the rapid growth of population and economic growth (Glaser et al., 1991). As of 2020, over 70 km^2 of land has been reclaimed in the New Territories and surrounding islands, accounting for about 7 % of the total land area (Feng and Xu, 2021; Ng, 2018). One of the significant challenges associated with reclaimed area is the long-term land subsidence due to soil consolidation of the underlying marine sediments and fillings (Glaser et al., 1991). This subsidence poses severe threats to the stability of constructed facilities, such as in the original northern runway at Hong Kong International Airport (HKIA). In 2020, HKIA has been developed into a three-runway system (3RS) to cater for the long-term air traffic growth. The expansion project commenced with urgent land reclamation efforts to prepare the area north to the original runway for civil use. Therefore, it is important to use specific reclamation methods to establish a stable and consolidated foundation before proceeding with any of further constructions on the bare lands.

The reclamation history of Hong Kong reveals a diverse range of technologies employed for land creation, primarily categorized into two main types: dredged and non-dredged reclamation methods (Kwong, 1997). The former requires to remove and dump all underlying marine deposits and then refill sand and rock materials, which has been used in the previous reclamation project HKIA (A. R. Pickles, 1998; Zhao et al., 2011). The compaction of landfill materials results in the localized settlement of HKIA project over the last two decades, with a maximum cumulative settlement of up to 40 cm at its north runway (Wu et al., 2020). The latter, non-dredged methods keep the soft marine sediment in situ and arrange preferential drainage paths in the marine mud to enable excess pore pressure to dissipate quickly (Kwong, 1997). This procedure can help to protect the environment against the releasing of mud pollutants and can swiftly establish a reclamation platform. However, the presence of marine mud increases the risk of subsidence and necessitates adequate drainage to achieve full consolidation, which results in the delays of the subsequent civil constructions (Huang et al., 2023). A notable example is the Penny's Bay Reclamation phase II (PBR2) project, which is a typical non-dredged case and experienced continuous and significant sinking, exceeding 1.6 m within three years following the completion of filling (Shi et al., 2019).

Due to the urgent construction schedule, non-dredged methods were adopted for the 3RS reclamation project. To expedite the consolidation process, two specialized techniques were utilized, i.e., deep cement mixing (DCM) and prefabricated vertical drains (PVD), depending on the land use purpose such as runway, factory area and environmental impacts. DCM is designed to improve the soil foundation for quick delivery, which mixes the original marine deposits with stabilization agents or blinder to realize in-situ solidification (Shen et al., 2023; Voottipruex et al., 2011). This method was applied over the runway regions (airplanes takeoff and landing) which is urgent to be used, as well as the area with contaminated mud pits (CMP) underground. The remaining area is improved by the conventional PVD method, which provides a shorter drainage path of the pore water and thus accelerates the consolidation process (Bo et al., 2015; Sakleshpur et al., 2018). It is noteworthy that the 3rd runway reclamation of HKIA is the first marine DCM project in Hong Kong and also represents the world's largest application of DCM in a single project (Henry Cheung et al., 2022). Despite the benefits and merits of the DCM method in controlling settlement being validated through site-specific trial embankment (Kravchenko et al., 2024), there is still a lack of quantitative assessment regarding the actual impact of DCM on consolidation settlement in practice. Nonetheless, the long-term impact of DCM on foundation stability remains insufficiently studied.

Ground subsidence is a crucial factor in studying the consolidation over reclamation areas. Synthetic Aperture Radar Interferometry (InSAR), as a powerful geodetic technique, has been widely used for ground deformation monitoring with millimeter-level precision (Aslan et al., 2018; Osmanoğlu et al., 2016; Xiao et al., 2022). Compared to conventional point-based measurements, such as ground leveling, Global Positioning System (GPS), extensometers, etc., (Tazlo Strozzi et al., 2001), InSAR offers extensive coverage and fine spatial details (Bokhari et al., 2023; Strozzi et al., 2003). Advanced time series InSAR (TSInSAR) techniques, such as persistent scatter interferometry (PSI) (Ferretti et al., 2001), distributed scatter interferometry (DSI) (Berardino et al., 2002; Ferretti et al., 2011), can provide deformation time series with millimeter accuracy and bi-weekly updates. These techniques have been successfully utilized in various applications including the ground subsidence monitoring in reclamation region, such as Italy (Teatini et al., 2005), Singapore (Bai et al., 2023), Turkey (Erten and Rossi, 2019), Korea (Kim et al., 2007), and China (Lenk, 2009; Zhao et al., 2019). Advances have also been made in interpreting the mechanism behind InSAR-derived subsidence related to oil consolidation in reclaimed land. On the one hand, InSAR measurements provide spatial details that help characterize deformation in relation to historical reclamation activities, geological features, and soil mechanisms (Park and Hong, 2021; Yang et al., 2018). For instance, subsidence at HKIA has been assessed through TSInSAR studies that incorporate the geological features of alluvial deposits (Jiang and Lin, 2010; Sun et al., 2018). These studies focus on subsidence rates grading and qualitative analysis of consolidation process. On the other hand, field investigations and macro-scale experiments have been applied to identify the stratigraphic structure and their contributions to land subsidence (Ciampalini et al., 2019; Yu et al., 2020). Microscopic pore and structure tests have also been conducted to examine the physical and chemical properties of soil, aiding in interpreting InSAR deformation of consolidation process at different phases of reclaimed lands (Hu et al., 2017; Shi et al., 2022b; Yu et al., 2021). However, these methods are often limited to in-situ experiments and lack the spatial details such as InSAR. Consequently, quantitative analysis of the consolidation process and soil compaction status at platform-wise are often missing, nonetheless offering actionable guidance for accurate soil reinforcement. Given the complexity of different reclaiming/improvement strategies, the consolidation process and the time-dependent soil status can vary largely from place to place at the 3rd Runway.

To study consolidation behavior from different reclamation techniques, it becomes essential to firstly characterize the differences, if any, between locations and time. Independent component analysis (ICA) is a mainstream blind source separation (BSS) technology that decomposes multivariate signals into independent non-Gaussian components (Hyvarinen, 2013). Benefited from the absence of assumptions about the underlying probability distribution of data, it is a powerful tool to separate and extract geophysical signals of interest from mixed source observations (Gualandi and Liu, 2021; Gualandi et al., 2015). The effectiveness of multi-source signal decomposition based on ICA has been validated broadly. For example, S. K. Ebmeier applies ICA to identify geophysical signals caused by tectonic, volcanic, and anthropogenic processes from InSAR deformation (Ebmeier, 2016). L. Maubant et al. uses ICA to separate atmospheric delays and tectonic deformation on time series data not corrected atmospheric phases (Maubant et al., 2020). Peng et al. utilizes ICA to extract independent signals with distinct spatiotemporal patterns from InSAR subsidence, such as long-term subsidence with seasonal rebound, linear deformation trend, the residual turbulent delay and other noise (Peng et al., 2022). Given the similar nature of mixed geophysical signals in consolidation deformation, ICA will be used to decompose the InSAR spatiotemporal data, thus characterizing the different physical processes in the 3rd runway. Another essential aspect is to understand the physical mechanisms behind varying consolidation patterns, from which more meaningful engineering indices and insights into future development trends can be reasonably inferred. The Terzaghi theory provides a foundational framework that describes consolidation process, primarily governed by the discharge of pore water under static loading (Radhika et al., 2017). To map the consolidation features of different reclamation techniques, it will be a promising attempt to incorporate Terzaghi principles with the InSAR ICA analytics. By synthesizing these two, unprecedented spatiotemporal details regarding the surface deformation and subsurface

consolidation status can be expected in the context of the 3rd runway project.

The aim of this paper is to investigate the spatiotemporal patterns and evaluate underlying consolidation process for the newly reclaimed HKIA 3rd runway, especially the discrepancy of consolidation status under the PVD and DCM reclamation methods. Firstly, we combine full-resolution persistent scatterers (PS) and distributed scatterers (DS) interferometry under the IPTA strategy to detect the spatiotemporal details of ground settlement spanning from September 2021 to October 2023. Then, we utilize ICA to separate different deformation sources driven by the distinct soil consolidation behavior. In addition, we incorporate the Terzaghi consolidation theory with the time series deformation measurement and underlay geology to infer the consolidation parameters and status at the 3rd runway. With equivalent spatial details as the InSAR data, the estimated consolidation processes have clearly determined the unequal effects of subsidence under different reclamation methods. This study provides invaluable and actionable suggestions on subsequent soil reinforcement planning on the 3rd runway and can advise optimal strategies for future reclamation projects.

2. Study area and data

2.1. The reclamation work and geology of HKIA 3rd runway

The scope of 3RS project is shown in Fig. 1, where the new reclaimed site (650 ha) is located at the north of the original HKIA (1248 ha) in west Lantau. The land formation work was commenced since May 2018 and completed in December (Henry Cheung et al., 2022). The reclamation areas were handed over to the follow-on contractors in phases for subsequent construction projects when reaching the required geological conditions. The main work of land formation includes the

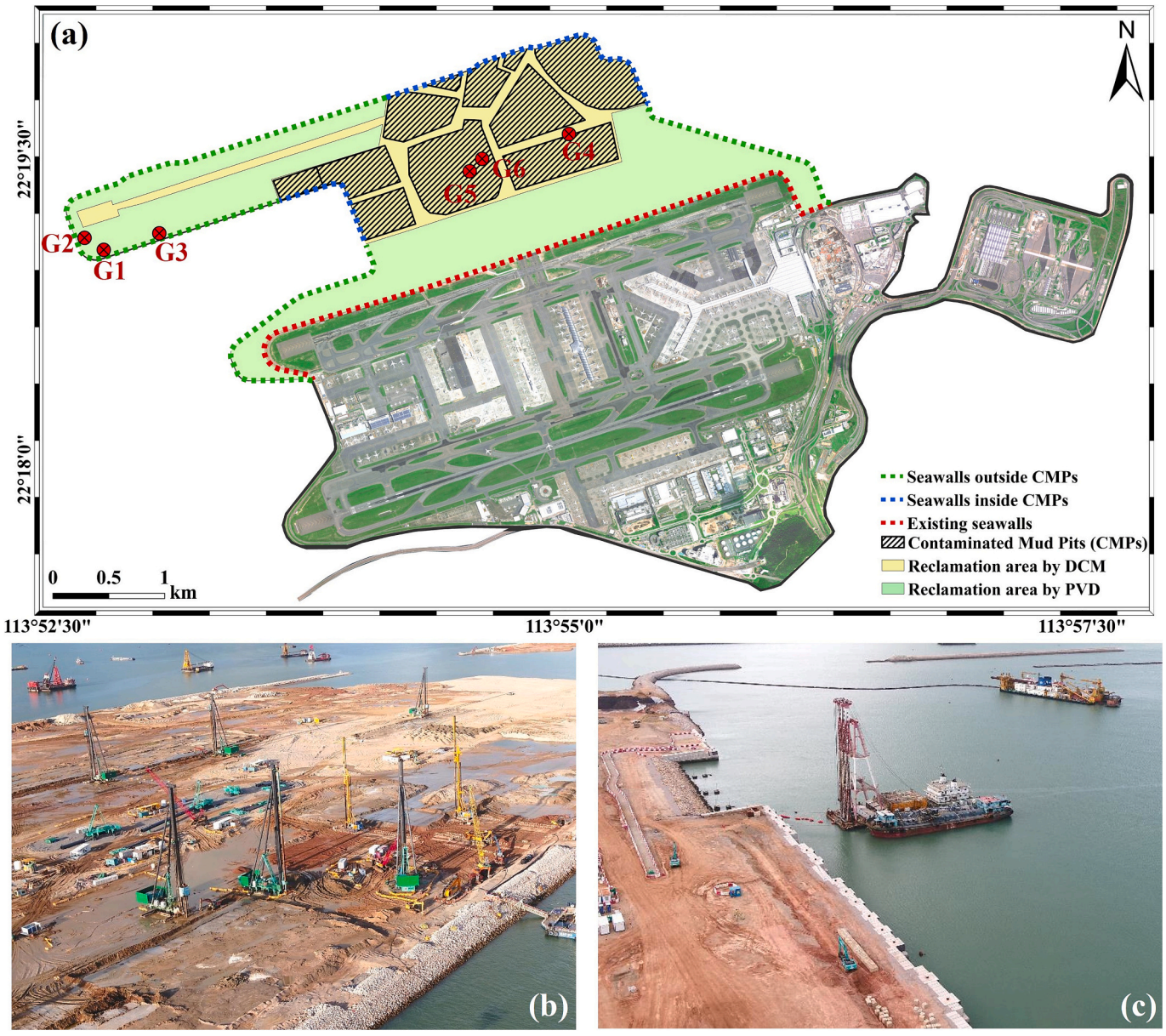

Fig. 1. (a) Partition map of ground improvement methods with DCM (light yellow) and PVD (light green) in the newly reclaimed site of HKIA. The background image of original HKIA is from Amap Global. The location of CMPs in the 3RS project is marked by black slant lines. The original seawalls are outlined in red dashed lines, and the seawalls outside and inside CMPs in the newly land are drawn in green and blue dashed lines, respectively. (b) and (c) are instance photos of DCM work and PVD work, respectively. (For interpretation of the references to colour in this figure legend, the reader is referred to the web version of this article.)

existing seawall modification (Red dash lines in Fig. 1), ground improvement of the underlying marine sediments, new seawall construction (green and blue dash lines in Fig. 1), filling and surcharge.

The existing seawall along the original north runway was modified to interface with the new land formation. The ground improvement methods were adopted variedly depending on the location (inside or outside the contaminated mud pits (CMPs)) and the designed land use in the future. The reclamation site is underlain by marine deposits (between 10 m and 20 m thickness) and alluvium (between 20 m and 25 m thickness), with average water depth of ~8 m. Roughly 320 ha reclamation area is featured as the CMPs with the thickness of about 27 m, which is indicated by black slashes in Fig. 1. Considering the environmental impacts, a non-dredged method called DCM was used to avoid the leak of contaminated material and water from CMPs. Except for the CMP areas, only the marine sediment beneath the 3rd runway was conducted by DCM in order to meet the more stringent performance criterion. Other than the DCM areas, the ground improvement was relying on PVD without dredging the marine mud, via which the consolidation process is accelerated by installing vertical wick drains to release retained pore water in the marine mud. The areas reclaimed by DCM and PVD methods are indicated by yellow and green polygons in Fig. 1a, and the schematic of DCM and PVD method are shown in Fig. 3. As of December 2020, the reclamation work was completed and some areas had been handed over for the following pavement in phases. The new seawalls for the airport expansion comprise sloping seawalls and vertical seawalls (only for some specific sections). To reserve the access channel for working ships, sectional seawall construction shall not commence until after the completion of the corresponding ground improvement work in that segment. Various filling materials including rock fill, public fill, sand fill, rock armour and graded filter layer were used to form the new land and seawalls. Especially for seawalls, they use the rock fill as the cores and form the protective layers by rock armour and graded filter layer. Temporary surcharging (primarily marine sand or public fill) was applied to facilitate consolidation process in its soft clay layer. The surcharge material will be delivered via hopper barge, pelican barge, trailer suction hopper dredger (TSHD) and off loaded into dump trucks.

The pavement work of the 3rd runway was executed and completed around September 2021. The 3rd runway was officially commissioned on 25 November (Henry Cheung et al., 2022). The relevant key time spots of the construction process of the 3rd runway are listed in Fig. 2b. The SAR images used in this study span from 11 September 2021 to 17 October 2023, which timely examined the initial deformation after the pavement completion.

2.2. Datasets and materials

In this study, we used 62 ascending Sentinel-1 A (Track 11) images spanning from September 2021 to October 2023 to monitor the land subsidence of HKIA. The GPS points used in this paper are located in the sites of Fig. 1a, which is applied to validate the accuracy of the InSAR derived deformation. The optical images of HKIA from Google Maps and Amap Global are used as the backgrounds for displaying the results. The layout and the geological information of underlying materials for the 3RS project are provided by the HKIA https://threerunwaysystem.hongkongairport.com/tc/three-runway-system/project-updates/the-third-runway-at-hong-kong-international-airport-commissions/ and The Hong Kong Legislative Council https://www.legco.gov.hk/yr19-20/english/panels/edev/papers/edev_ab.htm.

3. Methodologies

Fig. 4 illustrates the main data processing flow in this study, which includes three key blocks, i.e., combined processing of full-resolution PS and DS interferometry; deformation source decomposition and consolidation parameter estimation.

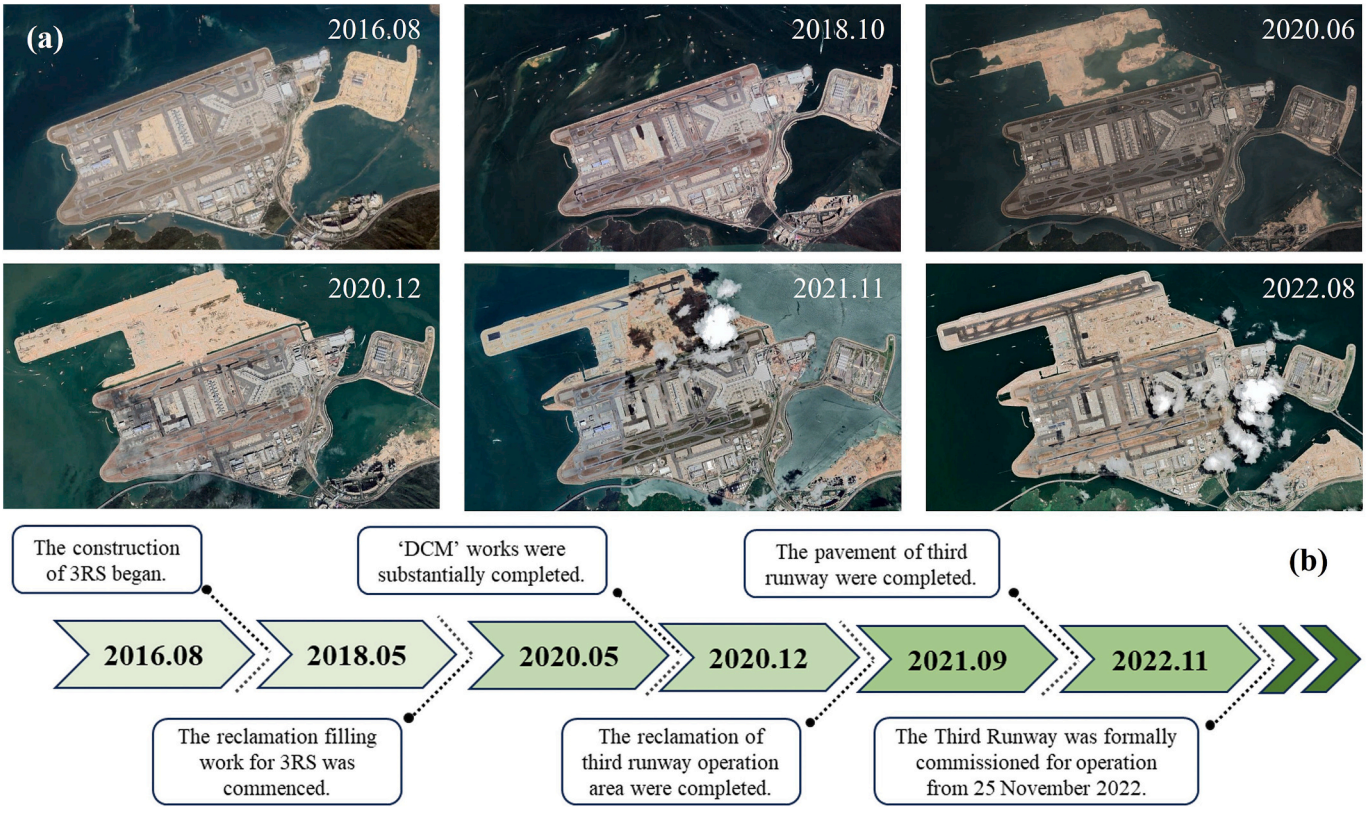

Fig. 2. (a) The construction stages of the 3rd runway of HKIA platform. The background images (with acquisition time) are from Google maps. (b) Timeline of the construction process at the 3RS project.

3.1. Combined processing of PS and DS

For newly reclaimed runways, phase coherence of SAR images is inevitably to be low due to the decorrelation from both bare soil coverage and "mirror reflection" of smooth asphalt pavement (Shi et al., 2018). To collect as much of deformation details, we integrate Persistent Scatter (PS) and Distributed Scatter (DS) interferometry technology to map the deformation of HKIA under the Interferometric Point Target Analysis (IPTA) strategy.

All full resolution interferograms are spatiotemporally filtered using homogeneous pixels to improve the phase quality (Jiang et al., 2015; Shi et al., 2022a). To mitigate the phase discontinuities, a phase-correlated pixel (PCP) clustering is used to identify PCPs with similar phase behavior, followed by an iterative phase linking (Shi et al., 2020). The selection of PCPs can be achieved by estimating the phase correlations between pixels, i.e.,:

$$P = \begin{bmatrix} 1 & \rho_{y_1y_2} & \rho_{y_1y_3} & \cdots & \rho_{y_1y_K} \\ \rho_{y_2y_1} & 1 & \rho_{y_2y_3} & \cdots & \rho_{y_2y_K} \\ \vdots & \vdots & \ddots & 1 & \vdots \\ \rho_{y_Ky_1} & \rho_{y_Ky_2} & \rho_{y_Ky_3} & \cdots & 1 \end{bmatrix} \tag{1}$$

$$\rho_{y_iy_j} = \frac{(y_i - \overline{y_i})^H \left(y_j - \overline{y_j}\right)}{\sqrt{(y_i - \overline{y_i})^H (y_i - \overline{y_i})} \sqrt{\left(y_j - \overline{y_j}\right)^H \left(y_j - \overline{y_j}\right)}}$$

where i and j are the pixel index, K is the number of tested pixels within the window, y is the complex phase vector, $\overline{y}$ is the arithmetic mean, H is the Hermitian conjugation, $\rho_{y_iy_j}$ is the complex correlation coefficient. To determine the similarity between neighboring pixels (i) and the central pixel (c) of the filter window, proper threshold can be set for $\rho_{y_iy_c}$ to group the PCPs (Shi et al., 2020). Afterwords, the coherence matrix of the PCP pixels was estimated:

$$\widehat{C} = \frac{1}{N_\Omega} \sum_{i \in \Omega} \overline{d} d^H \tag{2}$$

where $\widehat{C}$is the estimation of coherence matrix, $\overline{d} = [\overline{d}_1, \overline{d}_2, \ldots, \overline{d}_N]^T$ is the normalized complex observation of each pixel, N is the number of images, Ω is the PCP family with selected pixel number of N_Ω. The coherence matrix of the selected PCPs was then used to optimize the phase time series of DS candidates. In this paper, the phase optimization was realized by adopting the coherence weighted phase link, during which the temporal phase vector can be solved via an iterative process:

$$\widehat{\theta}_n^t = \angle \left\{ \sum_{m \neq n}^{N} \{\widehat{C}\}_{nm} exp\left(j\widehat{\theta}_m^{t-1}\right) \right\} \tag{3}$$

where $\widehat{\theta}$ is the phase to be solved, t is the iteration index, n and m are the image index, $\{\bullet\}_{nm}$ indicates entry at row n and column m. The advantageous of this spatiotemporal filtering was given in Fig. S1 in the supplement. Finally, the optimized phase was used to jointly solve the geophysical parameters of PS and DS pixels in the data stack. The stepwise, iterative regression analysis is performed based on the point targets to solve the time series deformation and remove atmospheric disturbance (Tabish et al., 2022; Werner et al., 2003). The combination of PS and DS points provides a more sufficient measurement density than using PS points only, as shown in the comparison in Fig. S2.

3.2. Spatiotemporal deformation from ICA

Deformation measurements from IPTA can be regarded as a set of linear combination of multisource contributions under various physical mechanisms. ICA is used to identify potential sources that are independent and non-Gaussian signals (Tharwat, 2020). This is achieved by maximizing the non-Gaussian of the sources and minimizing the mutual information of the sources (Gaddes et al., 2018; Pati et al., 2021). The relationship between the observed deformation signal $X_{t\times n}$ and the independent source signal $S_{m\times n}$can be described as:

$$X_{t\times n} = A_{t\times m} \bullet S_{m\times n} \tag{4}$$

where t is the number of SAR acquisition, n is the number of pixels and m is the number of independent components. $X_{t\times n} = \left[x_1^T, x_2^T, \ldots x_k^T, \ldots, x_t^T\right]^T$ is the observed InSAR deformation matrix and each column indicates the time series of InSAR deformation for each pixel. $A_{t\times m} = \left[a_1^T, a_2^T, \ldots a_k^T, \ldots, a_t^T\right]^T$ is the coefficient matrix of independent components and each column represents the temporal behavior of each independent component. $S_{m\times n}$ is the source matrix and each row represents the spatial behavior of each independent component.

In this study, we adopted the FastICA algorithm (Oja and Yuan, 2006) to decompose the InSAR time series. In this process, the variance explanation derived from PCA served as a reference to determine the number of major components retained for analysis, as shown in Fig. S3. This algorithm begins from the preprocessing of centering and whitening, which aims to reduce the dimensionally and transform signals into uncorrelated signals (Gaddes et al., 2018). FastICA algorithm uses a fixed-point iteration to derive the rotation matrix W, which represents the direction of maximum non-Gaussian:

$$S = W^T Z; A^{-1} = W^T \tag{5}$$

where A^{-1} is the inverse matrix of the mixed matrix A, and Z is the whitened matrix. Through the above iterative process, the source matrix S is determined.

3.3. Mapping underground consolidation status

Ground settlement in the 3RS evolves unequally in space and time due to the temporally asynchronous consolidation processes and spatially inconsistent reclamation methods. In general, the total settlement S can be contributed by three components, namely, immediate settlement S_i, primary settlement S_p, and secondary settlement S_s (Waheed and Asmael, 2023), as shown in Fig. 5a. Among them, S_i is the change or distortion of the soil shape under the applied stress (Tewatia, 2012), which is a relatively rapid process occurring within hours or a few days after filling/loading, and thus cannot be detected by the InSAR measurements. The S_p and S_s are the subsequent phases of time-dependent soil compaction processes. The former is a process of the complete dissipation of excess pore water pressure (e.p.w.p.), leading to the compression settlement of the soil layers, which is also regarded as the consolidation settlement (Lenk, 2009; Zeng et al., 2015). The latter refers to the gradual reduction of the soil volume due to the readjustment of soil particles without the water expulsion, which is also regarded as the creep settlement (Wahls, 1962). In other words, the consolidation can be expressed as a changed process from the moment the load is entirely carried by the water to the point the load is completely supported by soil (Duo et al., 2022). The Terzaghi's one-dimensional consolidation theory is widely used to describe such process (Al-Zoubi, 2008). The compaction is mainly regulated by two factors of the underlying materials: the permeability, which controls the rate of water removal from the soil and thus the rate of settlement at any time; and the compressibility, which controls the evolution of excess pore pressures and thus the duration of the consolidation (Shukla et al., 2013; Tewatia et al., 2011). Under the assumption that drainage and deformation occur only in the vertical direction, the volumetric variation of soil void at a specific period is directly related to the observed settlement that can be acquired from InSAR measurements (as shown in Fig. 5b):

$$\frac{Disp}{H} = \frac{\Delta e}{1 + e_0} \tag{6}$$

where *Disp* is the observed vertical settlement, H is the thickness of compressible soil, Δe is the changed void ratio and e_0 is the initial void ratio. Deformation obtained using the improved InSAR technique is along the satellite line-of-sight (LOS) direction. The vertical ground subsidence (soil compaction) is derived assuming the lateral soil motion is negligible in magnitude (please see Section 4.2). In the following, we modelled InSAR displacement with Terzaghi consolidation theory to map the underground consolidation properties, including the decay coefficient b, the consolidation time t_p, phased settlements S_p,S_c, and the consolidation degree *dg*.

3.3.1. The decay coefficient of soil compaction

Soil compaction depends on the rate of pore water discharge, which is determined by the soil permeability. Different types of soils tend to have disparate permeability rate. For granular soils, such as sands, the hydraulic conductivity is sufficiently large that consolidation process occurs quickly (Shafiee, 2008). For cohesive soils, such as clays, hydraulic conductivity is rather small and the consolidation process of a thick deposit may require years or even decades to complete (Zhang et al., 2019). In addition, secondary compression is insignificant for granular soils, whereas it can be substantial for cohesive soils (B. G, S., and B. A, M, 2012). Given the difficulties in obtaining detailed data related to the soil properties, we use the decay rate of the monitored vertical displacement to evaluate the consolidation rate. An empirical exponential decay function is used to simulate the time-dependent settlement:

$$disp(t) = a\left(e^{bt} - 1\right) \tag{7}$$

where $disp(t)$ is the time series vertical deformation, a is the coefficient representing the magnitude of the cumulative displacements, and $b \epsilon [-1, 0]$ is the decay coefficient characterizing the changed settlement rate. The parameters a, b are estimated based on iterative nonlinear least squares. Given an initial value a_0 and b_0, at the kth iteration, find an increment to minimize the object function. When the increment is small enough, the iteration can be stopped. Otherwise, it returns to the iteration process. The decay coefficient can be regarded as a qualitative measure of soil permeability. The larger the absolute value of the decay coefficient, the faster the rate decays, indicating a higher permeability of the underlying materials. Conversely, the smaller the values, the slower the change, indicating a weaker permeability of the underlying materials.

3.3.2. The transition time between consolidation stages

Based on the settlement curve, the turning point between primary consolidation and secondary consolidation can be regarded as the transition time spot t_p between the two physical stages. The transition time approximates the duration of primary consolidation, which measures the compressibility of the underlying materials. The lower the compression coefficient of the soil, indicating that the lower the compressibility of the soil, the stronger the ability against compress, and thus shorter the time to complete consolidation (Mesri and Feng, 2014). Given that the observation period begins after the pavement of the 3rd runway, the estimated t_p should be shorter than the actual consolidation time. The estimated primary consolidation time counting from the observation beginning (11 September 2021) can be calculated based on the fitted displacement curves:

$$t_p = \frac{ln((disp' - a)/ab)}{|b|} \tag{8}$$

where $disp'$ is the settlement velocity during different time period, acquired from the derivative displacement. Eq. (8) calculates the consolidation time corresponding to the period when the compaction rates slow down to a stable state. This stable state depends on a prior knowledge of the geodesy and subsidence monitoring records, which is believed to be under control when the rate decays to 10 mm/year (5 mm/year for some areas) (Liao et al., 2021; Wu et al., 2007).

3.3.3. Estimation of phased settlements

Given the temporally phased reclaiming activities, the InSAR vertical displacement can be separated into different settlement processes. Although the measurements all start at the first SAR acquisition time, each location corresponds to different settlement phases of its entire curves. Among them, there are many locations that have reached a steady state (already entered into the secondary consolidation phase) at the beginning of observation period (i.e., the settlement rate remains about or below 10 mm/year). The consolidation time and primary settlement of such points are both set to zero and the observed displacements, if any, at these points are considered directly as creep displacements. For the remaining areas, primary consolidation is obtained according to their consolidation time. Two catalogs are defined: 1) locations of which the primary consolidation can be completed within the InSAR observation time (2.1 years); 2) locations that have not completed primary consolidation within the observation period. For the first catalog, deformation time series are divided into two phases according to the transition time point. The monitored settlement before and after the transition point is regarded as primary settlement and secondary settlement, respectively. For the second catalog, the displacements outside the observation period are estimated by the integral of their rates over time. The sum of total monitored settlement and predicted settlement is considered as primary settlement of these points, while their secondary settlements are set as zero. Therefore, the ultimate primary settlement $S_p$and secondary settlement S_s can be calculated as:

$$S_p = \begin{cases} 0; & |\hat{v}| < 10mm/yr; \\ disp(t_p); & t_p < 2.1yr; \\ disp + \int_{2.1}^{t_p} \hat{v} dt; & t_p \geq 2.1yr; \end{cases} ; S_s$$
$$= \begin{cases} disp; & |\hat{v}| < 10mm/yr; \\ disp - S_p; & t_p < 2.1yr; \\ 0; & t_p \geq 2.1yr; \end{cases} \tag{9}$$

3.3.4. Mapping the consolidation degree of 3rd runway

For most cases, engineers are not interested in the amount of the consolidation settlement of a given point. Of more practical concern is the consolidation degree of the project at any time. This value, denoted by *dg*, is a measure of how much the reclaimed area has consolidated and thus it can be directly used to assess the consolidation status and advise subsequent civil constructions, or otherwise improvement plans (Lovisa et al., 2011). According to the Terzaghi theory, consolidation degree is expressed as the ratio between the dissipated e.p.w.p. and initial e.p.w.p. to assess the effectiveness of soil improvement work. However, due to the poorly measured physical variables, the degree of consolidation can be calculated using the ratio between the monitored settlement and the estimated ultimate primary settlement, as Eq. (10). This bridges the poorly measured physical process of e.p.w.p. dissipation into the measurable deformation from InSAR.

$$dg(t) = \frac{\Delta e}{e_0} = \frac{disp_t}{S_p} \tag{10}$$

where e_0 is the initial e.p.w.p., and Δe is the dissipated e.p.w.p. within a certain time, $disp_t$ is the observed settlement at time spot t and S_p is the estimated ultimate primary settlement. Specifically, when $S_p = 0$, the consolidation degree can be directly regarded as 1 as these points have reached stable status at the beginning of the observation period.

4. Results

4.1. Mean deformation rates of HKIA

The integration of PS and DS measurements has significantly improved the deformation details of the interferometrically low coherence 3rd runway acquired from InSAR. Fig. 6 presents the mean deformation rate of HKIA in the LOS direction. For the ascending S1 result, positive values (blue) represent the land uplift and potentially east to west deformation, and negative values (red) represent the land subsidence and potentially west to east deformation. We observe that the most areas of the original HKIA are stable and local significant deformation is detected on the central runway (the original north runway), with roughly settlement rate of 10-20 mm/year. The newly reclaimed area of HKIA 3rd runway is outlined by black solid lines in Fig. 6, and the critical area needed for operation of the 3RS project in November 2022 is marked as blue dashed lines. It is evident to see that the main subsidence zones are concentrated in the western area of the 3rd runway and the junction of the original airport and the new reclaimed land. The severe sinking area has the maximum subsidence rate exceeding 150 mm/year in the 3rd runway, marked as zone S with black dashed lines (Fig. 6). The spatial pattern of deformation is found to be highly correlated with the traditional PVD reclamation method (Fig. 1a), of which detailed discussion is given in Section 5.2.2.

In addition, to the east side of HKIA, the Hong Kong Boundary Crossing Facilities (HKBCF) also suffers considerable and distributed ground settlements. The HKBCF reclamation work commenced in January 2013 and completed in 2016. For the HKBCF, an innovative fully non-dredged reclamation is firstly used to construct the seawalls to form an artificial island with all the in-situ marine sediment left in place. Different to the 3rd runway, only traditional treatment of in-situ marine mud using band drain with surcharge was used in the main body of the reclamation fill. The interpretation of deformation pattern in the HKBCF has been well discussed in (Ma et al., 2024).

The vertical ground subsidence related to soil compaction is derived assuming the lateral soil motion is of negligible magnitude in the newly reclaimed site for the following analysis. To visualize the subsidence process in the critical area, we display the settlement status at different time spot in the Supplement Video S1. The dynamic process highlights the severe sinking area in the west block of the newly land, and the reason and mechanisms of this settlement will be discussed in Section 5.

4.2. Validation with in-situ GPS measurements

To evaluate the accuracy of InSAR measurements, we validated them with continuous GPS data, G1-G6 (Fig. 1). Among the GPS sites, G1, G2 and G3 are close to the western seawall with significant deformation, whereas G4, G5 and G6 are situated in the reclaiming land, where the construction is expected to be completed in 2024. The InSAR deformation points closest to G1-G6 are selected, and the LOS deformation is converted to vertical displacement for comparison, as shown in Fig. 7. All stations claimed great agreement between the InSAR time series and GPS measurements, with the maximum and minimum RMSEs to be 5.71 mm and 3.39 mm at G1 and G5, respectively.

In addition, the horizontal deformation at these points is also checked to demonstrate that the following analysis is carried out without being affected by horizontal deformation misinterpretation from LOS. The horizontal displacements of these points in the east-west (*E*-W) and north-south (N-S) directions are plotted as red dots and blue dots, respectively, in Fig. S5. The cumulative displacements of the points in the west block (G1, G2, G3) are all smaller than 20 mm both in E-W and N-S direction, much smaller compared to the vertical subsidence about 42 mm. The points (G4, G5, G6) outside the critical area have the cumulative displacement smaller than 30 mm in the E-W direction, and they have larger cumulative displacement in N-S direction of −38.8 mm, −26.7 mm, 123.3 mm, respectively. The horizontal deformation occurs in construction areas and taxiway edges where the surface soil is not completely fixed, and the ongoing civil works and traffic loading could have introduced more horizontal motions (Ma and Jiang, 2024). However, the contribution factors from vertical, N-S and E-W directions to LOS are 0.73, −0.14 and − 0.66, respectively. Given the significant subsidence and the looking geometry, the displacements in the horizontal directions have limited effects on our vertical conversion. Therefore, the LOS measurements can be reasonably converted to subsidence for our subsequent consolidation analysis.

4.3. Spatiotemporal deformation from ICA

In this study, there are 62 SAR acquisitions with 341,470 pixels at each acquisition, constructing the input mixed source data. The PCA results suggest that the first five components explained 91.09 % of the data variance, with 78.72 %, 8.04 %, 1.88 %, 1.39 %, and 1.06 %, respectively (Fig. S3). Fig. 8 shows the spatiotemporal patterns of the first three independent sources (corresponds to the three largest PCs), and Fig. S4 presents the spatiotemporal patterns of residual components (i.e. IC4 and IC5). The spatial responses of each IC are normalized to score values of [−1,1] (Fig. 8a-c, Fig. S4a-b), and time series of three ICs acquired by multiplying the temporal eigenvectors by the corresponding score values are plotted in Fig. 8d and Fig. S4c-d. The score values quantify the spatial contribution of each independent signal, while the IC time series show the deformation process with different temporal characteristics. By interpreting the spatiotemporal patterns of ICs, the spatial pattern of IC4 is rather noisy and its high-value is mainly distributed in few points where these areas are still under construction with much artificial disturbance outside the critical operation area (Fig. S4a). This may come from construction disturbance (where you can observe land subsidence after March 2023 in Fig.S4c), and this is not the consolidation signal of concern. IC5 is widely distributed in spatial and fluctuated within the displacements of 5 mm temporally, except for a few outlines (Fig. S4b and d). This may come from other unconsidered sources, e.g., rainfalls, tides, and atmospheric disturbance, etc., but not the continuous compactions from consolidation. Therefore, we only retain the first three signals (88.64 %) for analyzing the consolidation deformation.

It is evident that the predominant subsidence pattern can be attributed to the synergy of IC1 and IC3 with different weights. IC1 exhibits an exponential decay pattern in the temporal evolution, and is widely distributed in the newly reclaimed area without distinct clustering patterns. This indicate the deformation source was probably due to the transition from primary to secondary consolidation processes of the filling/underlays across the site. In Fig. 8d, the decay signal of IC1 can be observed to weaken in June 2022 and start to level off. However, the IC3 shows a close-to-linear deformation trend over the observation period, indicating continuous ground subsidence. The IC3 score map highlights that the most affected area with such sinking trend is in the western taxiway zone. However, some minor linear subsidence was also found in the 3rd runway pavement. Apart from these two ICs, the temporal eigenvectors of IC2 show the remarkable periodic deformation pattern. Such behavior of IC2 is related to thermal effects, especially on those linear structures such as the buildings and bridges. For example, the IC2 score map (Fig. 8b) highlights an opposite deformation pattern at the ends of the bridge blocks, with one end having positive score values and the other end having negative score values. This phenomenon is due to the thermal expansion and contraction of concrete, during which both ends of the concrete block featured with opposite motion directions. In Fig. 9b, we select two points C1 and C2 (Fig. 8b) to showcase the relationship between the periodic deformation and the temperature changes. The IC2 deformation trend corresponds exactly to that of seasonal temperature variation, which confirms our explanation on this source. This type of deformation is not of interest in this study, therefore is discarded in the following analysis.

4.3.1. The IC1 deformation source: fast compaction of surficial filling

IC1 curve demonstrates the later period primary consolidation for the filling/underlays, experiencing a shorter time to achieve a stable state. This component likely indicates the rapid compaction process of a surficial filling layer, which makes no significant difference spatially between the DCM and PVD area in the 3rd runway. To further confirm the source of this component, we average deformation time series of IC1 at locations with considerable IC1 scores greater than 0.5 in the 3rd runway reclaimed by DCM and PVD, respectively. Comparison between the time series is given in Fig. 9a, where the IC1 time series is also listed. Need to note that the time of reclamation completion is same for the selected points at the DCM and PVD areas, meaning they were undergoing synchronized consolidation period. Apparently, the temporal patterns of this component between DCM and PVD areas remain consistent, in which the settlement in the DCM reclaimed land (an average of −24.1 mm) is basically identical to in the PVD reclaimed land (an average of −24.5 mm). This signifies IC1 stems from the compaction process of the same surficial filling layer of the DCM and PVD area (Fig. 3), rather than the underlay marine mud layer with different DCM/PVD treatments.

4.3.2. The IC3 deformation source: continuous land sinking

IC3 highlights the continuous (linear) subsidence concentrated mostly in the west taxiway area and distributed across the reclaimed site. As can be seen from Fig. 9c, strong correlation is found between IC3 score and the monitored deformation in Fig. 6. The IC3 is claimed to be the major source leading to those critical subsiding zones as monitored currently. On the other hand, the distribution of subsidence rates is spatially coherent with the reclamation methods. Fig. 9d compares the histograms of deformation rates between DCM and PVD reclaimed land. The PVD reclaimed land has a higher concentration of averaged sinking rates exceeding 40 mm/yr. However, the statistics show that most of DCM area is situated at low rates, indicating that the desired ground stability is achieved for further security operation. More details about the comparison of the effects of DCM and PVD methods will be discussed in the following section.

5. Discussion

5.1. Shrinking boundaries of subsidence

Our analysis on the phased settlement pattern has revealed shrinking of those significant subsidence areas. We separate the deformation into two sections: from11 to 09-2021 to 25–11-2022 (before the official operation of the 3rd runway) and from 29 to 11-2022 to 19-10-2023 (after the official operation of the 3rd runway). Fig. 10 compared the spatial patterns of the cumulative vertical displacement, the IC1 displacement and the IC3 displacement before and after the operation of the 3rd runway. In the spatial domain, the overall subsidence pattern has been significantly reduced in spatial from the first 13 months (Fig. 10 a1) to the last 10 months (Fig. 10 b1). In particular, no evident subsidence was found at the pavement area after its operation. According to the IC1 exponential decay deformation, the widespread IC1 displacement at the reclamation was completed before the official operation (Fig. 10 a2), this could be sourced from the quick compaction of a filling/existed layer. On the other hand, the IC3 linear settlement terminated in most locations of the site after the runway operation but continued in Zone S (Fig. 10 a3-b3). Therefore, we believe that IC3 has dominated the spatial pattern of the overall subsidence after the operation of the 3rd runway. The mechanism of such unsynchronized consolidation is complicated (see discussions below) and it is necessary to arise concerns on the settlement of Zone S for future developments.

5.2. Factors regulating the consolidation process

5.2.1. Phased reclaiming stages

The reclamation work was conducted in three stages, as shown in Fig. 11a. The first block of land completed the reclamation work before the quarter of 2019, and then the eastern and junction (with the original airport) area were completed in the third quarter of 2020, followed by the western runway area in the fourth quarter of the same year. This construction process can be visually observed from the optical images of Fig. 2. Fig. 11b provides a statistical view of the settlement rates during different construction stages, which offers a sketchy understanding on how the construction sequence affects the settlement. The scatters with different colors show the distribution of deformation rates in different construction stages. The distribution of deformation rates differs greatly among stages, and settlement rates exceeding 100 mm/year are concentrated in the region reclaimed in the third construction stage. It is known the later the reclamation is completed, the earlier the consolidation phase stays. The western area is at least three months behind the consolidation phase of the eastern area. This is also consistent with the fact that the severe sinking is located where the reclaiming was lastly completed. Fig. 12 shows the cumulative vertical deformation profiles along the blue dashed lines outside and inside the pavement area (AA'(Fig. 10 a1) and BB' (Fig. 10 b1)). Need to note the two profiles at the same distance are essentially at the same construction stages. From the profile in the pavement (BB'), where all constructed by DCM, the settlement of western part is more than twice that of eastern part due to the lag of consolidation process. However, in addition to the timing

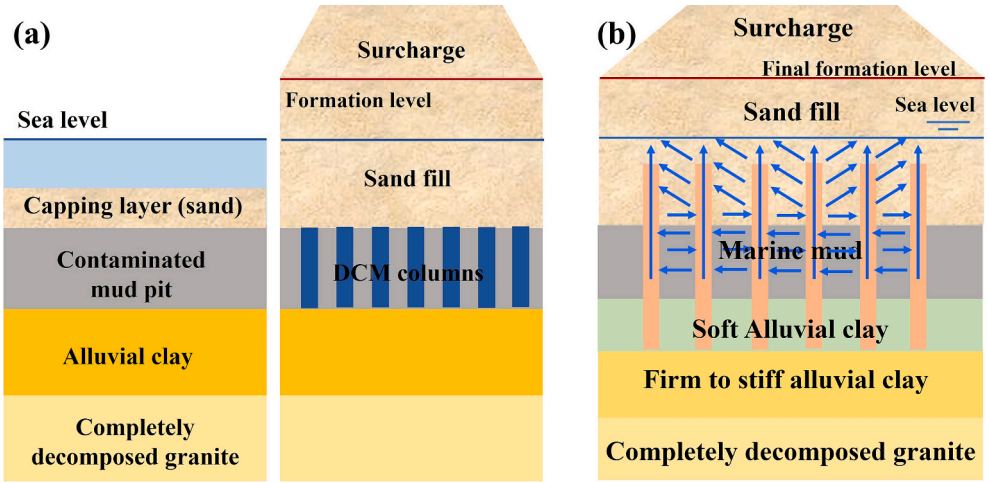

Fig. 3. Schematic of reclamation methods of (a) deep cement mixing (DCM) and (b) prefabricated vertical drains (PVD) for the 3rd runway area.

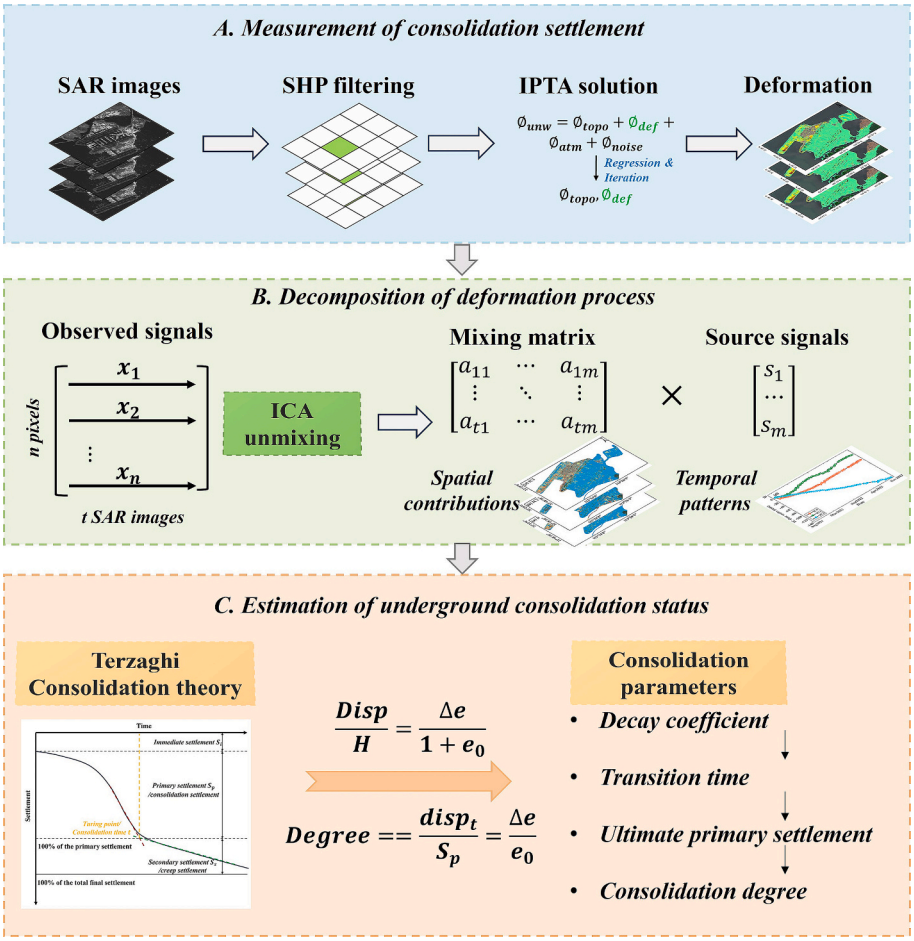

Fig. 4. Flowchart of research methodologies applied in this work.

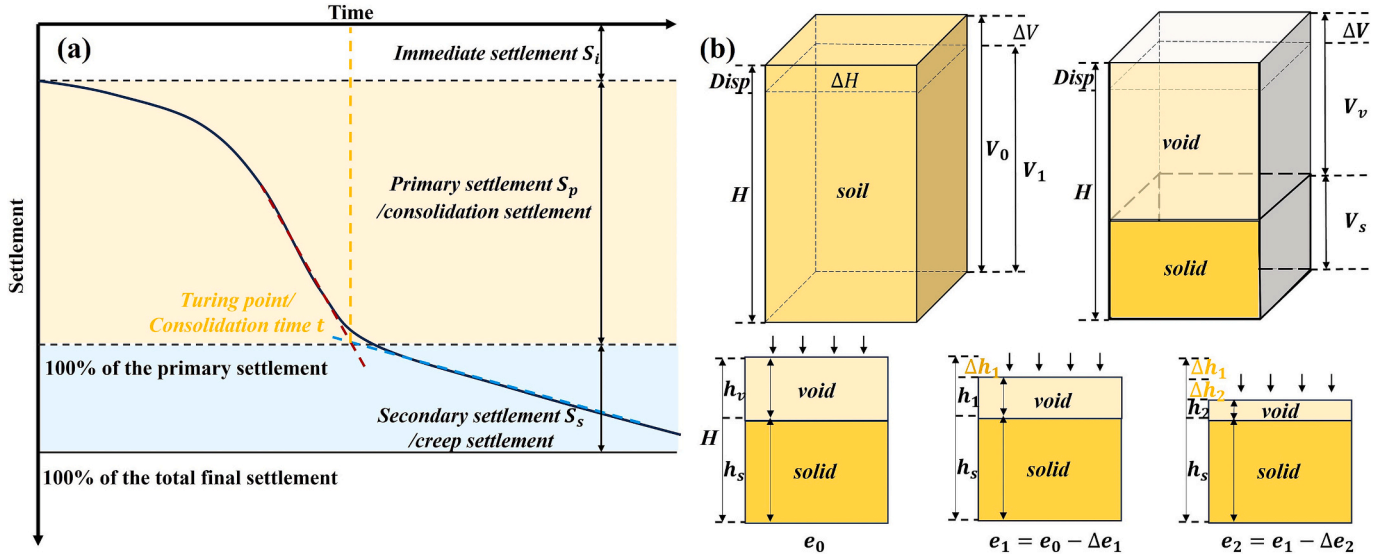

Fig. 5. Principals of the Terzaghi theory. (a) The characteristic curve of phased settlement. (b) The schematic diagram presents the process of reduction in volume of soil by the expulsion of pore water, where ΔH represents the height of the compressed soil layer in the subsidence process, which is identical to the observed settlement *disp*, h_v and h_s are the height of all underground compressible drainage layers and uncompressible solid layers, respectively. ΔV is the volume of the subsided soil layer; V_v is the volume corresponding to all compressible drainage layers and V_s is the volume corresponding to uncompressible solid layers; Δh_1, Δh_2 are the height of compressible soil layer (i.e. the observed settlement) during different time intervals and h_s is the height of uncompressible solid layers; $e_0, e_1, e_2, \ldots$ are void ratio related to different time intervals, $\Delta e_1, \Delta e_2, \ldots$ are the changed void ratio during different time intervals of the consolidation process.

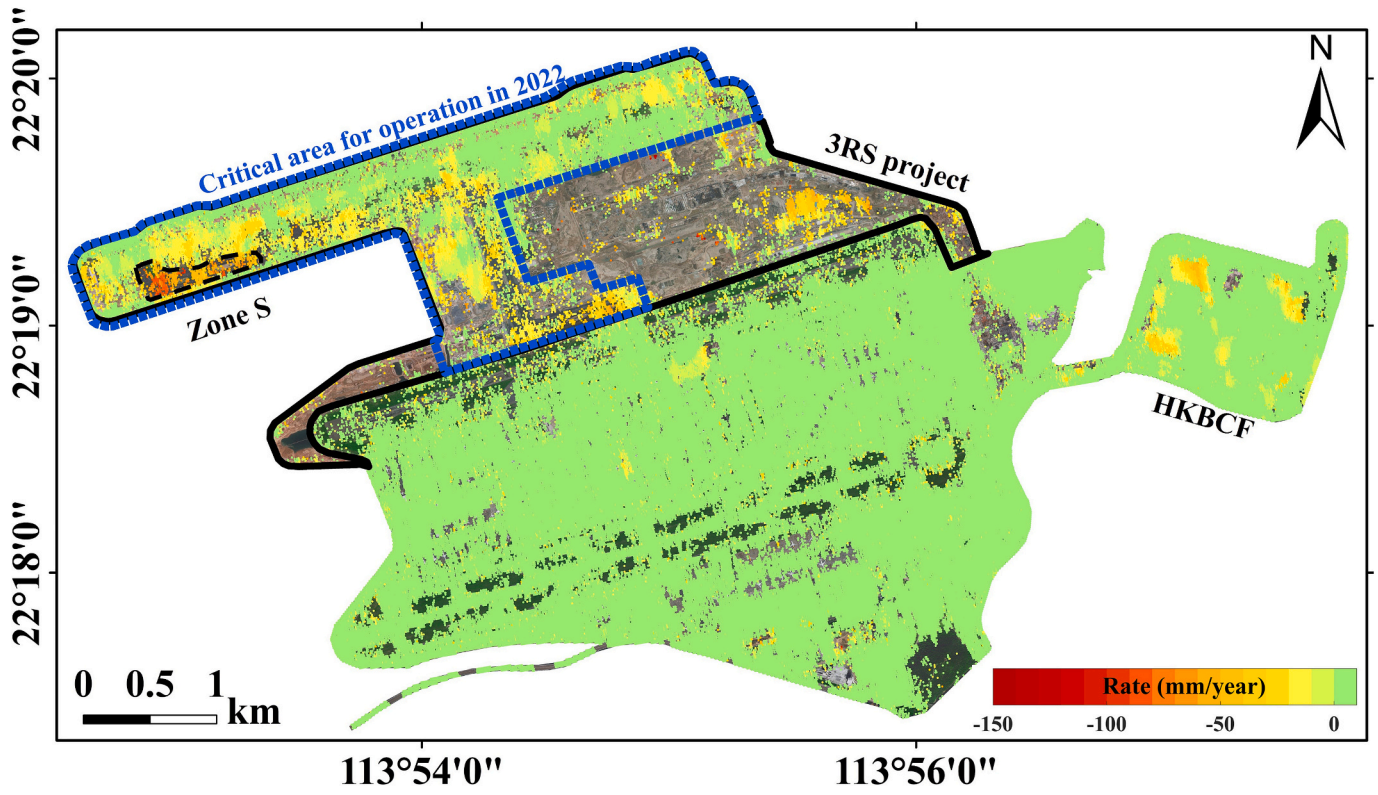

Fig. 6. Mean deformation rate of HKIA after the 3rd runway pavement. The black solid line indicates the newly reclaimed land of HKIA and the blue dashed line indicates the critical area needed for operation of the 3RS in November 2022. The black dashed line highlights the severe sinking area (Zone S) in the 3RS project. The area with sparse deformation points (outside the critical area of the newly land) has been under construction during the observation period and will continue until 2024. The dynamic process of the monitored settlement of the critical area can be seen in Supplement Video S1. (For interpretation of the references to colour in this figure legend, the reader is referred to the web version of this article.)

difference, more discrimination between the west and east displacement was find in AA', along which the reclamation method applied is different.

5.2.2. *Reclamation methods*

The construction timing can lead to different phases of consolidation but the same mechanism. However, within the same construction stage, the consolidation behavior can be immensely different between the PVD and DCM methods. As shown in the profiles (AA' and BB') of Fig. 12, the maximum settlement of PVD reclamation region is three times as that of DCM reclamation region. This result demonstrates that DCM reclamation provides higher efficiency on controlling the later land settlement. To quantify such decelerated settlement, the decay coefficient b is mapped in Fig. 13a. The greater the absolute value of the coefficient (close to 1), the faster the decay and the more efficient the consolidation.

Stable areas such as the seawall and the earlier reclaimed pavement mainly show a slight decay trend with $b \in$ (0- -0.1), and the remaining areas are mainly deformation areas, with b of (0−−1). We compiled the relationship between the average settlement rates and the decay coefficient under the DCM and PVD reclamation methods, see Fig. 13b. To avoid the interference from the variable of different construction process, we focus on analyzing the deformation points solely in the third reclamation stage. Assuming that the underlying materials are similar in their physical nature, the consolidation should be at the same phase under a common construction stage. However, our data shows significant difference in the settlement of DCM and PVD reclaimed areas. The whiskers outside the box represent 1.5 times interquartile range (IQR) of the settlement rates corresponding to different decay coefficients (Fig. 13b). When the absolute values of decay coefficient are less than 0.5, the settlement rate of PVD reclamation land is approximately 150 mm/year, five times that of DCM reclamation land. Similarly, when the absolute values of decay coefficient are greater than 0.5, the settlement rate of PVD reclamation land is approximately 70 mm/year, two times that of DCM reclamation land. This means at all levels of decays the DCM undergoes much small settlements than the PVD. In addition, Fig. 13b shows many discrete values outside the 1.5 IQR in PVD reclamation, which corresponds to severe settlement locations. The decay coefficients of these locations concentrate in (0, −0.1), indicating significant and continuous land sinking, and the settlement rate decays slowly.

To demonstrate the decreased subsidence process in time series, Fig. 13c-e averaged the settlement at locations with different decay levels of $b \in$[−0.1, −0.3], [−0.5, −0.7], [−0.7, −1], respectively. The circles and triangles represent the DCM and PVD methods, respectively. For the slow decay of $b \in$[−0.1, −0.3], the settlement rate has not stabilized in the last two months of the observation period for the PVD reclamation. It is plain to take longer to stabilize for these PVD reclamation land, i.e., the settlement rate of PVD land is 1.9 years later than that of DCM land to slow down to less than 50 mm/year. For the moderate and fast decay levels ranging from −0.5 and − 0.1, the settlement rate in the DCM reclamation stabilizes roughly 0.5 and 0.2 years earlier than that in the PVD reclamation, respectively. The statistics have proved that DCM has a faster stabilization rate at all coefficient intervals, indicating a more efficient consolidation than the PVD. More details quantifying the consolidation time are given in the next section.

5.3. *Consolidation time under different reclamation methods*

Asynchronous reclamation stages and different reclamation methods give rise to diverse consolidation responses. The slackening settlement rate varies in different blocks, which leads to the differentiation over time to complete primary consolidation. To evaluate the current consolidation status and infer the future, it is fundamental to estimate

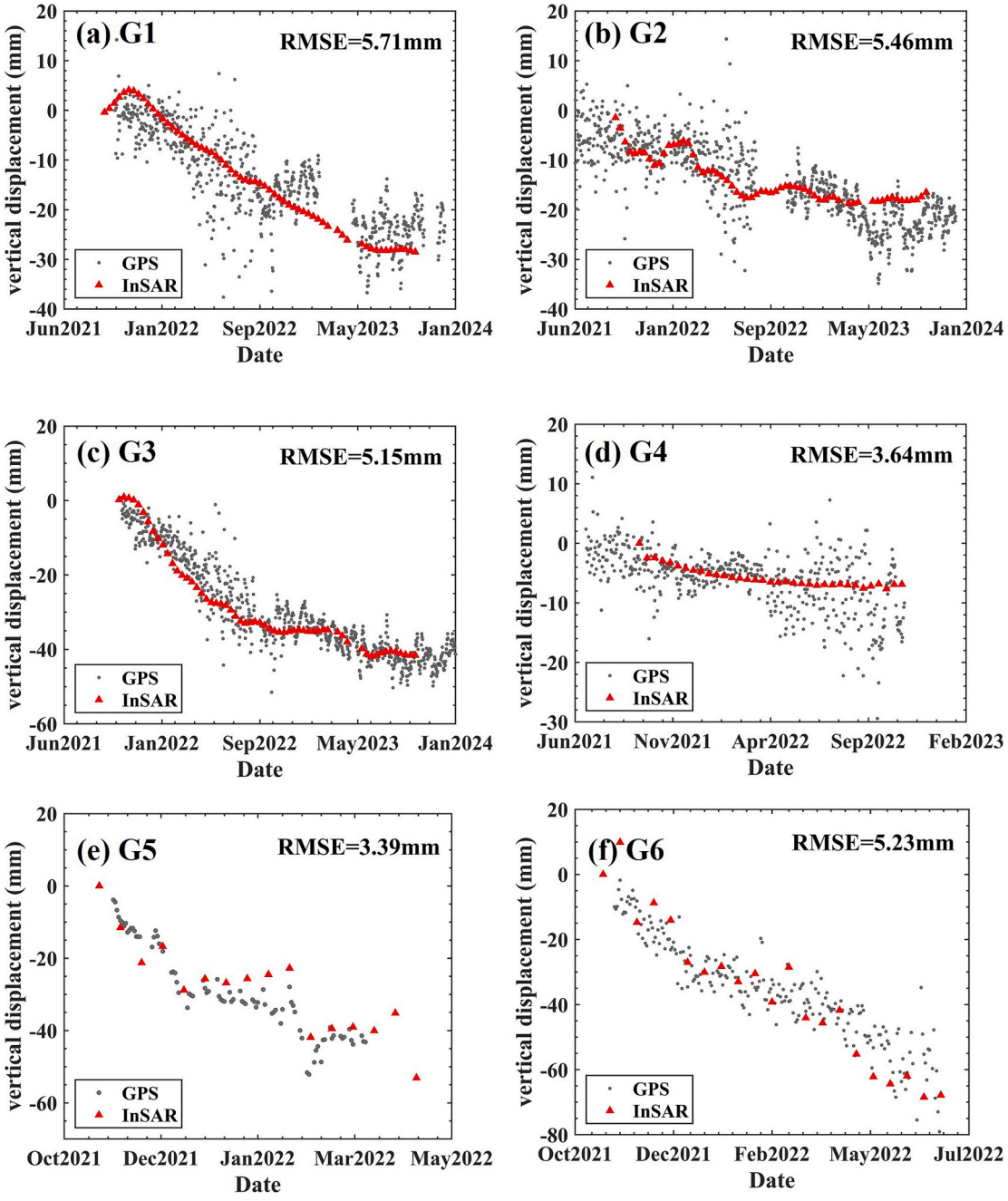

Fig. 7. Validation of the InSAR results based on GPS data at stations G1-G6 marked in Fig. 1. The gray dots and red triangles represent GPS and InSAR deformations, respectively. The RMSEs between them are marked in the subplots. (For interpretation of the references to colour in this figure legend, the reader is referred to the web version of this article.)

the transition time between primary and secondary consolidation processes. Civil constructions are normally made during and/or at the later period of secondary consolidation when foundations are (approaching) stabilized. Fig. 14a shows the estimated consolidation time taken to complete the primary consolidation since the completion of pavement of the 3rd runway (September 2021). The eastern block is the first to be reclaimed and is basically consolidated in the first 0.5 years of the observation time. Our estimation has outlined the area entering to the secondary consolidation phase prior to the 3rd runway operation (November 2022) and proved the efficiency of DCM in accelerating consolidation process. Longer consolidation time can be found concentrated in the last reclaimed area during the third stage (western block). In particular, the lengthiest time is mainly located in the PVD area, where approximately additional three years beyond the monitoring period is expected for these areas to enter into the creep phase, as shown the reddish points in Fig. 14a. During the last two months of the observation period, the settlement rate in these areas still reaches 60 mm/year. Temporal velocities under these two soil improvement methods are demonstrated by profiles of T_1T_1' (DCM) and T_2T_2' (PVD), where an immediate slowdown was found in DCM (Fig. 14c). In fact, the pavement area had essentially reached stable within 1.5 years (T_1T_1'), whereas the taxiway (T_2T_2') has not yet stabilized until the observation ends. Fig. 14b summarizes the initial (the first two months of the observation period, v_0) and terminal (the last two months of the observation period, v_t) velocities of DCM and PVD in greenish and red-orange colour, respectively. The statistical distribution shows the superiority of DCM reclamation method in slowing down the settlement

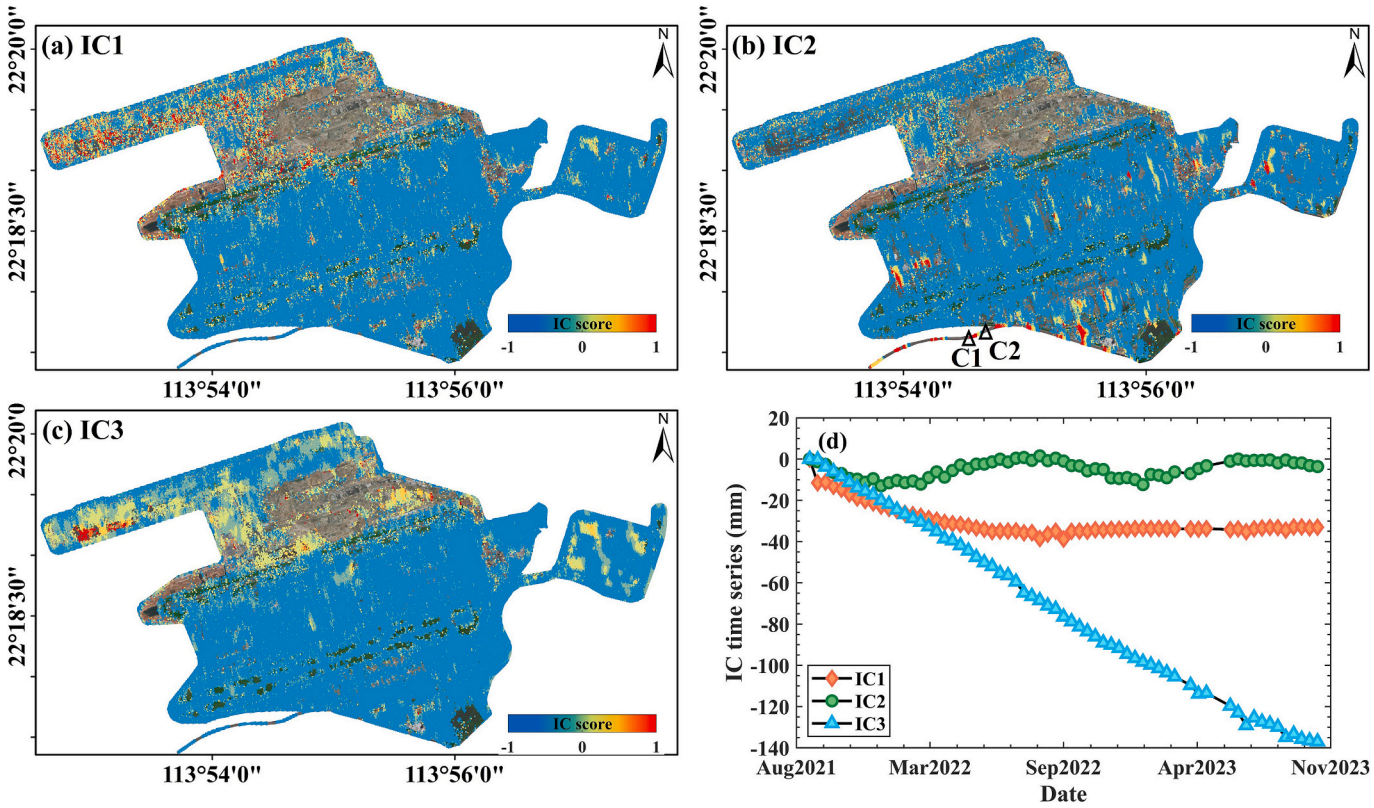

Fig. 8. ICA analytic results from the InSAR time series data. The spatial score maps of (a) IC1, (b) IC2, and (c) IC3, and (d) their corresponding eigenvectors (time series). Two points of C1 and C2 at the ends of the bridge are marked as black triangles in (b).

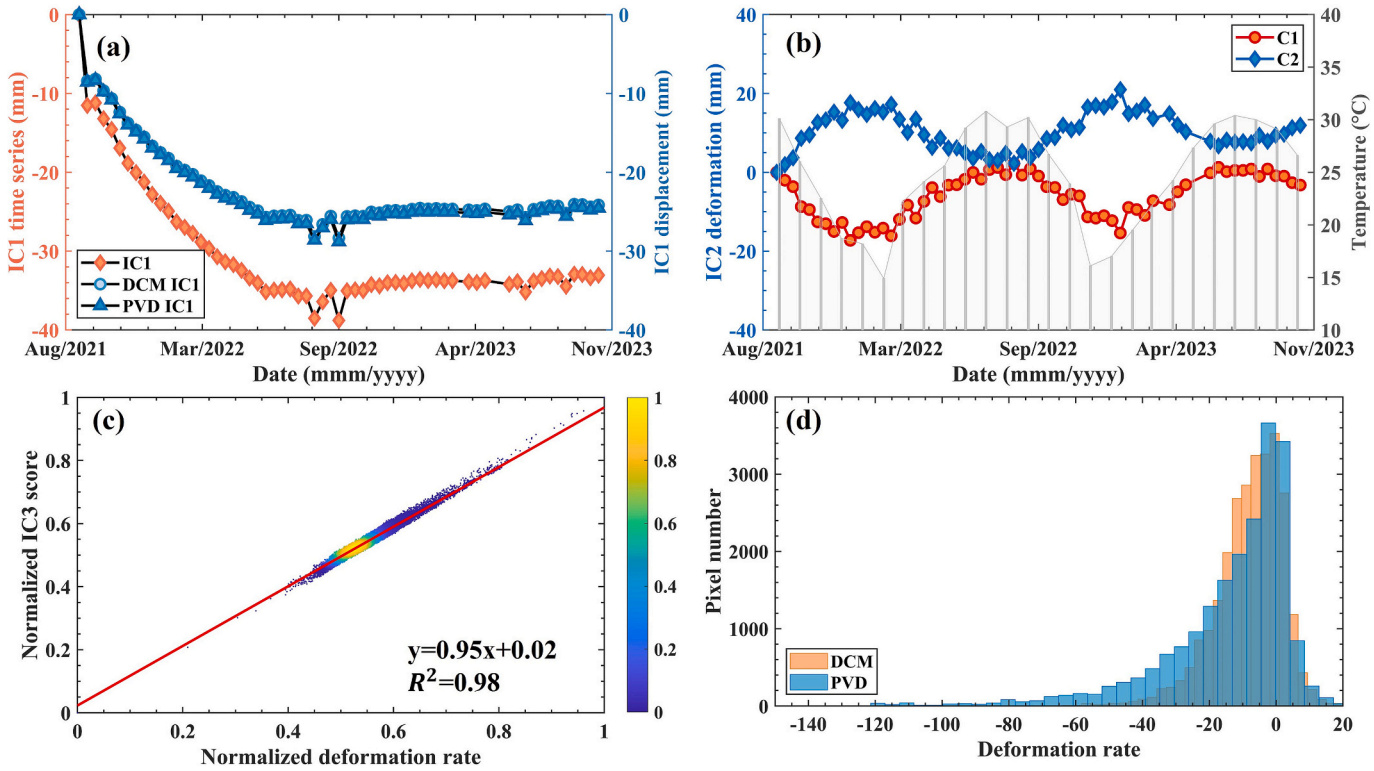

Fig. 9. (a) The comparison between IC1 time series (orange rhombus curve) and representative exponential decay displacements of the DCM (light blue circle curve) and PVD (dark blue triangle curve) locations at the same reclaiming phase. (b) Temporal correlation between the temperature and deformation of point C1 (orange circle curve) and C2 (blue rhombus curve) marked in Fig. 8b. (c) The kernel density between the normalized deformation rates and the normalized IC3 scores in the reclaimed area. (d) The histograms of deformation rates in the reclaimed land filled by DCM (orange) and PVD (blue), respectively. (For interpretation of the references to colour in this figure legend, the reader is referred to the web version of this article.)

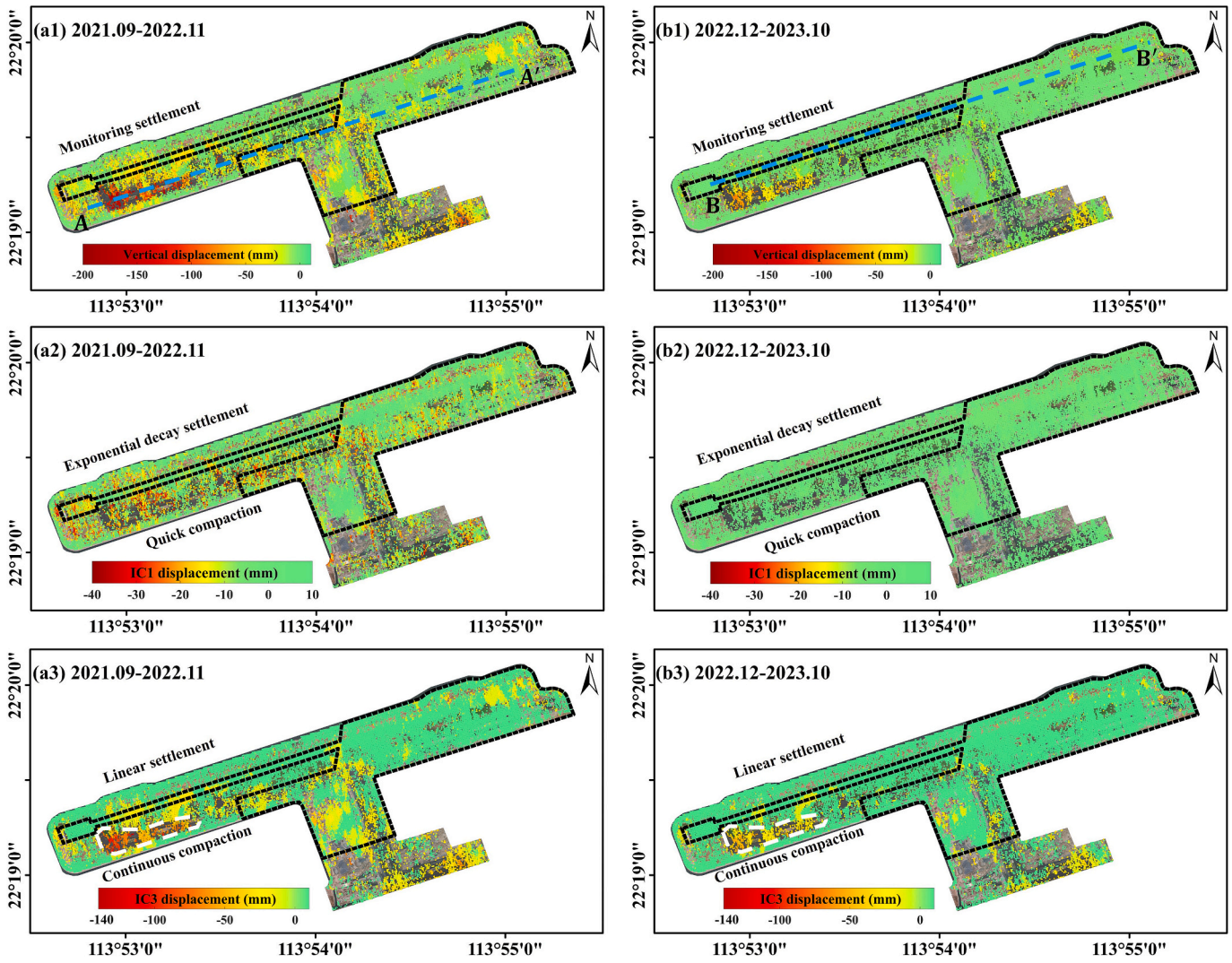

Fig. 10. The comparison of spatial pattern of subsidence before (the left column) and after (the right column) the 3rd runway operation. From up to bottom are the vertical displacement, the IC1 displacement and the IC3 displacement, respectively. The black dashed lines in each subfigure indicate the DCM reclamation region and the white dashed lines in (a3) and (b3) indicate the severe sinking area (Zone S). The blue dashed lines *AA′* and *BB′*are the profiles along the taxiway and runway, respectively. (For interpretation of the references to colour in this figure legend, the reader is referred to the web version of this article.)

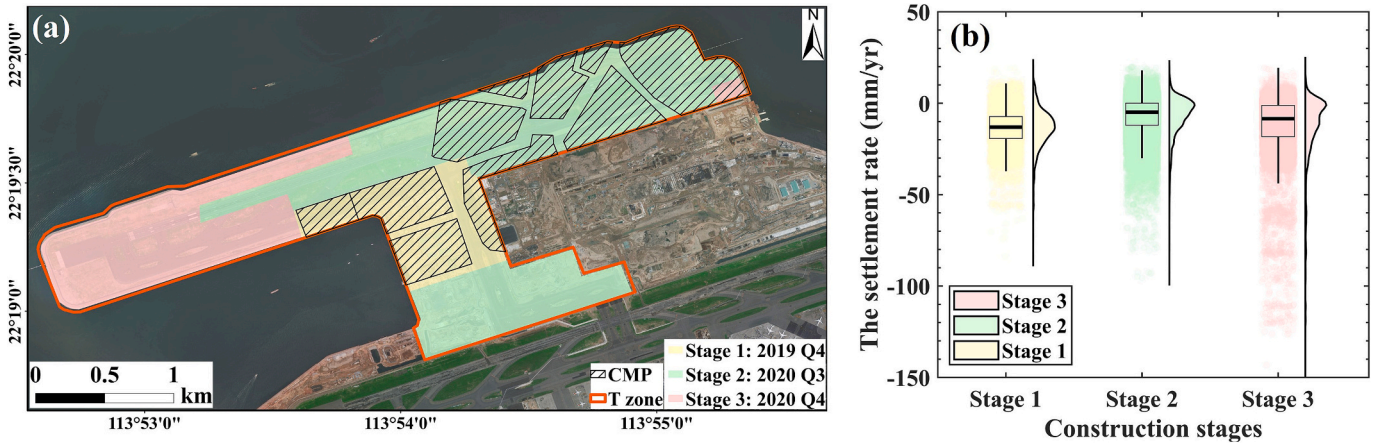

Fig. 11. (a) The spatial distribution of reclamation work completed at different stages. (b) Group comparison of raincloud plot showing the subsidence rates at different reclamation stages. The three construction stages from early to late are represented by yellow, green and pink, respectively. Kernel density plots depict the frequency of different rates while scatterplots display the settlement rates. Boxplots indicate the median, upper and lower quartile, and the length of vertical lines range the 95 % confidence interval. Yellow, green and pink colour corresponds to phased construction stages, respectively. (For interpretation of the references to colour in this figure legend, the reader is referred to the web version of this article.)

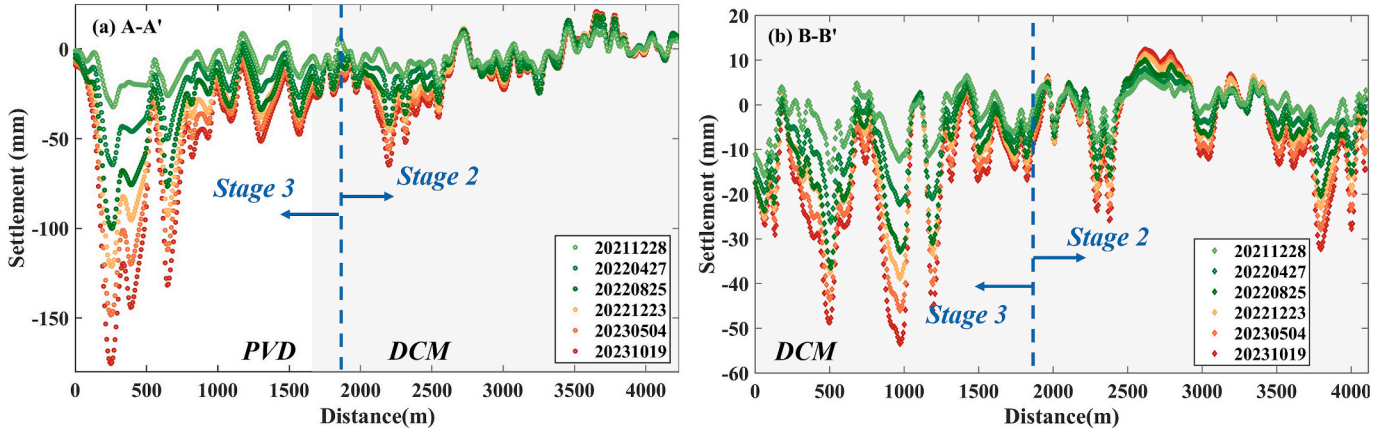

Fig. 12. The settlements along the profile directions of (a) A-A' and (b) B-B′ marked in Fig. 10. The green and orange lines are the cumulative deformation before and after the 3rd runway operation, respectively. The gray and white background indicates the ranges reclaimed by the DCM and PCV, respectively and the blue dotted lines indicate the spatial demarcation of reclamation time. (For interpretation of the references to colour in this figure legend, the reader is referred to the web version of this article.)

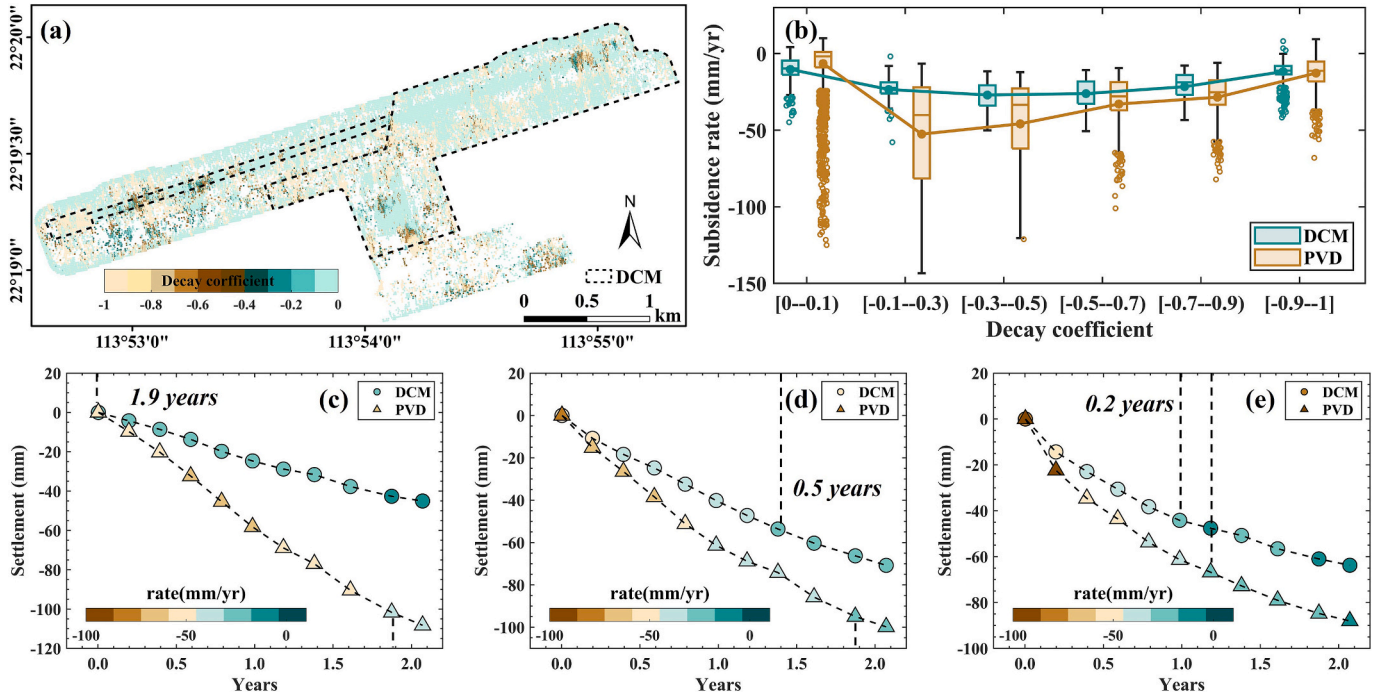

Fig. 13. (a) The spatial distribution of consolidation decay coefficients. The black dotted polygon indicates the region reclaimed by DCM method and the remaining region is reclaimed by PVD method. (b) The grouped boxplots show the comparison of subsidence rates representing different consolidation decay levels between DCM and PVD methods. In the box, the central line indicates the median and the filled point indicates the mean. The edges of the boxes show the interquartile range (IQR), and the whiskers indicate all data within 1.5 IQR of the nearer quartile. Data points beyond 1.5 IQR are marked as hollow dots, which highlight the distribution of points with fast subsidence rates. (c)-(e) demonstrate the mean settlements of deformation points with different intervals of consolidation decay coefficients [−0.1, −0.3], [−0.5, −0.7], [−0.7, −1], respectively. The circles indicate DCM method and the triangles indicate the PVD method. The colors of marks indicate the settlement rates every two months.

rate.

Further, Fig. 14d plots the average temporal evolution of settlement rates for the deformation points with different initial velocity ranges of [−120,−100] mm/year and [−80, −60] mm/year, respectively. The trends suggest the velocity decreases most rapidly in the initial 0.4 years, with slowing pace of deceleration thereafter. Under the same initial velocity range, DCM reclaimed land (green circles in Fig. 14d) achieves stabilization more quickly than the PVD (orange triangles in Fig. 14d). This advantage of DCM method is more pronounced at higher initial velocities. That is, although the range of initial velocities for DCM method varies spatially, the deformation points all leveled off within 0.4–0.7 years. Unlike this, the PVD method reduces the initial velocity to 20 mm/year for slow initial velocities (60–80/mm/year) within 1.2 years, whereas fast initial velocities (larger than 100 mm/year) still remain 30 mm/year at the end of observation period (longer than 2.1 years). The results also suggest the initial velocity v_0 has little effect on the attenuation process of velocity in DCM region, whereas it does have a significant effect in PVD region. We conclude such characteristics of the changed velocity are closely related to the principles of foundation improvement under the two reclamation methods. PVD has to drain the excess pore power water from the weakly permeable marine sediments, and thus the primary consolidation needs to spend more time. In

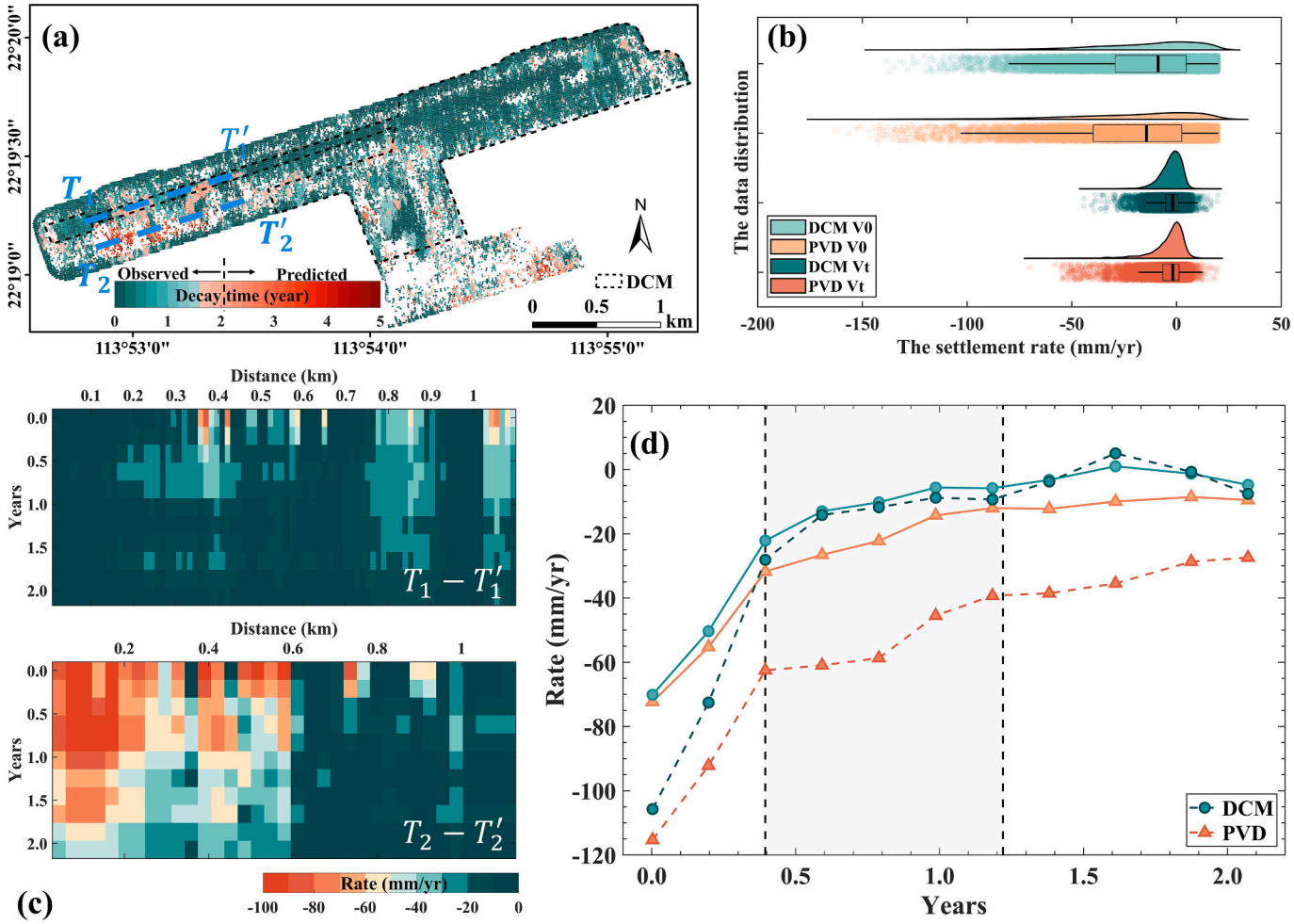

Fig. 14. (a) Estimation of transition time between the consolidation processes. (b) The distribution variation of initial and final settlement rates during the observation period. (c) The profiles of the time varying settlement rates along the directions of $T_1 - T'_1$ and $T_2 - T'_2$ in subplot (a). (d) Temporal evolution of average settlement rates of deformation points with different initial rates. The green circles indicate DCM method and the orange triangles indicate the PVD method. Moreover, the solid and dashed lines indicate the initial rates in the interval of [−100, −60] and [−120, −100], respectively. (For interpretation of the references to colour in this figure legend, the reader is referred to the web version of this article.)

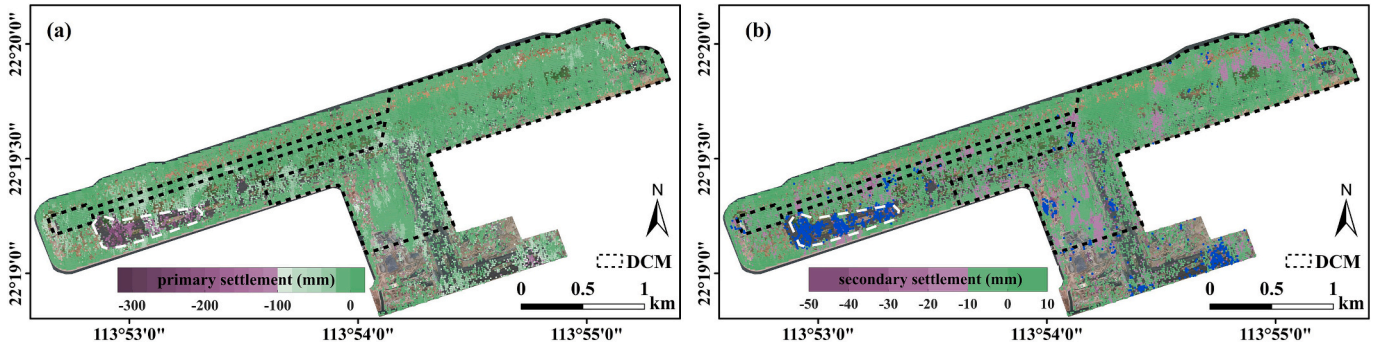

Fig. 15. (a) The primary consolidation, with settlement larger than 100 mm shown in distinguished colour. Locations completed the primary consolidation within the observation period: settlement values derived from InSAR measurements; Locations failed to complete the primary consolidation within the observation period: settlement values refer to combination of InSAR observation and the predicted settlement beyond the observation period. (b) The secondary consolidation, with settlement larger than 10 mm shown in distinguished colour. Locations completed the primary consolidation within the observation period: settlement values derived from InSAR measurements; Locations failed to complete the primary consolidation within the observation period: set as 0 (blue points in (b)). The white dashed lines indicate the concentration zone of points failed to complete the primary consolidation, and the black dashed lines indicate the scope of DCM reclamation land. (For interpretation of the references to colour in this figure legend, the reader is referred to the web version of this article.)

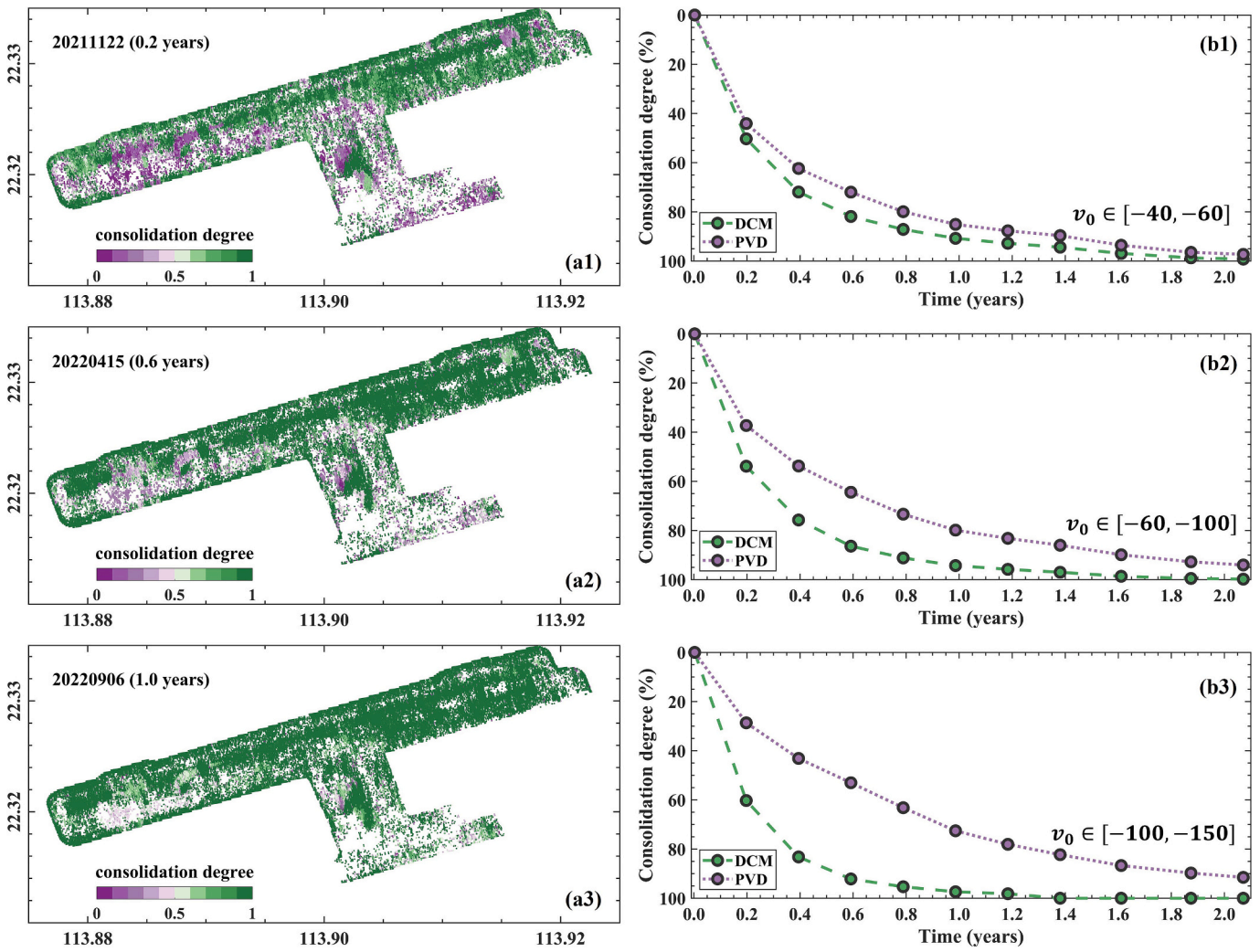

Fig. 16. Estimation of the underlay consolidation degree in the reclaimed site. The subplots (a1) - (a3) in the left column show the consolidation degree of underground substances in 0.2 years, 0.4 years and 1.0 years, respectively. The subplots (b1) - (b3) in the right column show the average consolidation degree of deformation points with different initial velocities of [−40, −60], [−60, −100], [−100, −150], respectively. The green and purple circles correspond to DCM and PVD reclamation method, respectively. (For interpretation of the references to colour in this figure legend, the reader is referred to the web version of this article.)

Table 1
The consolidation time difference of the deformation points with the same initial velocity between DCM and PVD reclamation method. The deformation points with the same initial velocity means at the same consolidation stage.

Deformation points in different initial velocities	Consolidation time difference	
	Mean (PVD)-Mean (DCM) (year)	Max (PVD)-Max (DCM) (year)
$v_0 \in [-150, -100] mm/year$	1.39	3.42
$v_0 \in (-100, -60] mm/year$	0.83	1.65
$v_0 \in (-60, -20] mm/year$	0.08	0.93
Range	**0.08–1.39**	**0.93–3.42**

contrast, the DCM directly applied loading concentrates on columns, which results in a decrease in the vertical stress acting on marine deposits. The sustenance of columns is therefore effective in shortening the consolidation time. The shortened consolidation time of DCM compared to PVD are summarized in the Table 1, which lists the mean and maximum difference of deformation points with different initial velocities. Note that all the selected deformation points are at the third reclamation phase, and the same initial velocity range is used to minimize the effects of different consolidation phases due to reclamation works. This table clearly shows the more advanced the consolidation stage (the larger the initial velocity), the more predominance for DCM reclamation method (the larger the consolidation time difference). In addition, we prefer the mean difference of consolidation time to compare two reclamation methods as it even better to reflect the universalities than the particularity of maximum values. Therefore, we estimate DCM could shorten the consolidation time by 0.08–1.39 years compared to the conventional PVD method for the same consolidation phase.

5.4. Estimating phased settlement of the 3rd runway

The primary and secondary consolidation settlement can be mapped using the timing estimated in section 5.3. The mapped consolidation settlement can be much less than authentic consolidation settlement due to limited observation period. Note that the mapped primary consolidation shares the same start time (11th Sept., 2021), whereas the end time is different from place to place. While the start time for the mapped secondary consolidation is the end of primary consolidation and the end time is the last SAR acquisition (19th Oct., 2023). For the locations that have completed the primary consolidation during the observation period (the estimated time shorter than 2.1 year), InSAR deformation is segmented into two parts based on the estimated transition time of different consolidation phases. Whereas for the deformation points

failing to complete the primary consolidation until the end of InSAR observation (the estimated time longer than 2.1 year), we integrate the total InSAR observation with the predicted settlement beyond the observation period. Therefore, the primary consolidation settlement of these points is larger than the observed settlement, and their secondary consolidation settlement is not predicted (set as 0, marked as blue dots in Fig. 15(b)). Results of the mapped primary and secondary consolidation settlements are presented in Fig. 15.

According to their spatial patterns, the western block mainly experienced primary settlement, while the eastern mass mainly experienced secondary settlement during the observation period. The eastern reclamation area experiences primary settlement for a relatively short period, and thus enter into the creep stage, with most of the secondary settlement during the observation period being smaller than 10 mm, and the maximum localized settlements being less than 30 mm. The western taxiway suffers the manifest primary settlement, with the maximum settlement larger than 300 mm. These areas are mainly concentrated in PVD reclamation zone and have little or no creep settlement within the limited observation time, which is accord with the forward described pattern. The primary consolidation behavior is greatly alleviated in DCM reclaimed land as DCM columns have the effect of controlling settlement by transferring the load from marine deposits to DCM columns. Further, we speculate that DCM reclaimed land will not experience significant secondary settlement due to the improvement of hydraulic conductivity for underlying materials. However, we should persistently focus on the secondary settlement in PVD reclaimed land because it may be long-lived owing to poor hydraulic conductivity for unreinforced underlying materials.

In order to quantify the ability to control the settlement between DCM and PVD methods, we list the mean and maximum settlement ratios between the deformation points with different initial velocity ranges in DCM and PVD reclaimed land, respectively (Table 2). These ratios indicate DCM reflects absolute advantage in resisting the settlement during the early consolidation phase (i.e., the larger the initial settlement rate and the smaller the ultimate primary settlement ratio). Therefore, we believe DCM columns could effectively control the settlement to 29 %–83 % of the PVD method in the same consolidation phase.

5.5. Mapping underlay consolidation degree for the 3rd runway

The consolidation degree is used to translate the ultimate primary settlement into a measure to evaluate the consolidation progress, which avoids the ambiguities of using settlement amount to evaluate the consolidation status due to unsynchronized reclamation phase and divergent reclamation ways. Figs. 16 (a1) - (a3) give the consolidation degree (with 1 to be completion of primary consolidation) of the underlying substances in different time spots, and the purplish and greenish points indicate the consolidation degree smaller and larger than 0.5, respectively. The results highlight that consolidation degree in the eastern blocks of the 3rd runway are much higher than that in the western blocks at the same time points, which has proven the influence of asynchronous reclamation phases discussed in Section 5.2.1. When the observation reaches one year, the consolidation degree in the DCM land of the western runway basically reaches 0.5, while the consolidation degree in the PVD land is mostly below 0.5. Further, we characterize the time series of consolidation degree using locations with different initial velocity ranges of [−40, −60], [−60, −100], [−100, −150], as shown in Fig. 16(b1) – (b3), respectively. Note that the selected deformation points are located at the newly reclaimed land in the third reclamation phase. We can observe that DCM reclamation has achieved higher consolidation degrees than PVD at the same time. The efficiency of DCM is reflected in such that the greater the initial velocity, the more pronounced advantage for DCM applications, which enables the fast transfer of the land to civil usage.

To intuitively assess the consolidation behavior of this project, readers are referred to the dynamic description of supplementary Gif. S1, which shows the evolution of consolidation degrees (from 0 to 1, with 1 being the completion of primary consolidation) at different time spots. Two orange profiles along the taxiway (D_1D_1') and runway (D_2D_2') are shown in the upper graph of Gif. S1. The lower subplots of Gif. S1 compare the dynamic evolution process of consolidation degree of PVD and DCM reclamation land in the same construction phase. For the newly reclaimed land, DCM method has consolidated more quickly than PVD method. Therefore, the paved runway has basically completed the primary consolidation in the last of the observation period.

Table 2
The ultimate primary settlement ratio of the deformation points with the same initial velocity between DCM and PVD reclamation method. The deformation points with the same initial velocity means at the same consolidation stage.

Def. points in different initial velocities	Ultimate primary settlement ratio	
	Mean (DCM)/Mean (PVD) (%)	Max (DCM)/Max (PVD) (%)
$v_0 \in [-150, -100] mm/year$	29	14
$v_0 \in (-100, -60] mm/year$	45	34
$v_0 \in (-60, -20] mm/year$	83	56
Range	**29 % ~ 83 %**	**14 % ~ 56 %**

6. Conclusions

In this study, we investigated the multi-mode consolidation process at the newly reclaimed HKIA 3rd runway. The integrated PS and DS has successfully retrieved the ground deformation of the low coherence land from September 2021 to October 2023 with meter-level spatial details. The measurements helped identify continuous subsidence zones concentrated at the west part of the reclaimed site, and more detailed deformation sources were separated using ICA analytic. For the first time, we have quantified the spatiotemporal settlement processes under the two reclamation methods of DCM and PVD, respectively. In addition, the Terzaghi consolidation theory was incorporated with the detailed remote sensing data to map the time-dependent underground consolidation status, including the consolidation time, ultimate primary settlement and consolidation degree. The methods and analysis used in this study can be applied to other reclamation projects with similar ground improvement methods. For the 3rd runway particular, we summarize the following conclusions and implications:

1. The subsidence pattern mainly presents local regions during the monitoring period. The most severe subsidence center is located in the western section, where the largest subsidence rate exceeding 150 mm/year. For most of the 3rd runway area including the pavement region, the ICA analysis shows that exponential decay settlement of the filling/underlay has leveled off before its official operation, while the linear deformation (continuous sinking) exists even after the official operation, especially in the PVD reclaimed land. Although the continuous subsidence was not affecting the pavement zone, we recommend that timely monitoring should be assigned over these areas to evaluate if any reinforcement actions is needed in the near future.
2. The spatiotemporal features of land subsidence are well correlated with the reclamation stages and methods. Land reclaimed first tends to consolidate earlier than land reclaimed later, as is evident on the eastern section. In addition, DCM reclamation method is superior to PVD reclamation method in terms of consolidation efficiency. Most of the DCM reclaimed land in the 3rd runway has fully completed the primary consolidation and entered into the secondary consolidation within the monitoring period. However, the sinking area of PVD reclamation land has not slow down to a desired rate and still requires years before a stable foundation can be made.

3. DCM works have the effectiveness in ground improvement by reducing consolidation time and controlling consolidation settlement. For the deformation points with the same initial states, DCM reaches a steady rate around 0.08–1.39 years faster than PVD method. For the estimated ultimate primary settlement, DCM reclamation land made it possible to control the settlement to 29 %–83 % of PVD method. In addition, the Terzaghi theory has converted the settlement into consolidation degree, which is a more intuitive indicator describing the consolidation process of the underlying. The result also indicates that DCM has completed a higher consolidation degree than that of PVD in the same period. The consolidation degree links the observed settlement with the properties of underlay, making it more practical for engineering applications such as reinforcement planning.
4. Although both DCM and PVD belong to non-dredged method, DCM improves the physical properties of marine deposits by adding cement to form stiff columns. However, PVD only removes pore water from the sediment through vertical drains, which requires sufficient drainage to accelerate the consolidation process. This method tends to take a longer time to complete consolidation owing to the lack of powerful sustentation. In contrast, the 3rd runway case proved a quite successful practice of the DCM, of which the accelerated consolidation is from the stiffness of DCM columns instead of the hydraulic contributions of PVD. In this regard, the DCM method should be the preferred option for reclamation projects that require fast/urgent delivery to civil use, especially good reference for future reclamation plans in Hong Kong.

To summarize, this study enhanced our understanding of the multi-mode consolidation process of the newly reclaimed 3rd runway of HKIA, via the comprehensive integration of satellite remote sensing, ICA analytics, consolidation theory and ground geology data. These findings offer meter-level details of the underlay consolidation status, which should be useful to suggest more accurate and reliable actions for soil improvement (if necessary) and subsequent civil constructions. The results will also be useful for future reclamation projects, e.g. the ongoing land reclamation for Tung Chung new town extension, and the Lantau Tomorrow Vision.

Supplementary data to this article can be found online at https://doi.org/10.1016/j.rse.2024.114561.

CRediT authorship contribution statement

Zhuo Jiang: Writing – original draft, Visualization, Validation, Methodology, Investigation, Conceptualization. **Guoqiang Shi:** Writing – original draft, Supervision, Resources, Methodology, Funding acquisition, Conceptualization. **Songbo Wu:** Writing – original draft, Supervision, Resources, Conceptualization. **Xiaoli Ding:** Supervision, Resources, Funding acquisition, Conceptualization. **Chaoying Zhao:** Writing – original draft, Supervision, Conceptualization. **Man Sing Wong:** Writing – original draft, Resources, Funding acquisition. **Zhong Lu:** Writing – original draft, Supervision, Conceptualization.

Declaration of competing interest

The authors declare that they have no known competing financial interests or personal relationships that could have appeared to influence the work reported in this paper.

Acknowledgement

This work is supported in part by the National Natural Science Foundation of China (Grant No.42304052), the Research Grants Council of Hong Kong (Grant No. 15229523) and the UGC-PolyU Grants (Grant No. P0050333, No. P0042898 & No. P0045896). M.S. Wong thanks the funding support from the General Research Fund (Grant No. 15603923 and 15609421), and the Collaborative Research Fund (Grant No. C5062-21GF) from the Research Grants Council, Hong Kong, China; and the funding support from the Research Institute for Sustainable Urban Development, The Hong Kong Polytechnic University, Hong Kong, China (Grant No. 1-BBG2). Sentinel-1 A images are provided by European Space Agency (ESA) and achieved by the Alaska Satellite Facility, GPS measurements are collected from field surveying, geology data of the reclamation project is from HKIA https://threerunwaysystem.hongkongairport.com/sc/three-runway-system/project-updates/the-third-runway-at-hong-kong-international-airport-commissions/ and The Hong Kong Legislative Council https://www.legco.gov.hk/yr19-20/english/panels/edev/papers/edev_ab.htm.

Data availability

Data will be made available on request.

References

Al-Zoubi, M.S., 2008. Consolidation characteristics based on a direct analytical solution of the Terzaghi theory. Jordan J. Civil Eng. 2 (2), 91–99.
Aslan, G., Cakır, Z., Ergintav, S., Lasserre, C., Renard, F., 2018. Analysis of secular ground motions in Istanbul from a long-term InSAR time-series (1992–2017). Remote Sens. 10. https://doi.org/10.3390/rs10030408.
B. G, S., & B. A, M, 2012. A Preliminary Numerical Study of the Improvement to Secondary Settlement Offered by Granular Columns. In: Proceedings of the International Conference on Ground Improvement & Ground Control, pp. 685–690.
Bai, Z., Wang, Y., Li, M., Sun, Y., Zhang, X., Wu, Y., Li, Y., Li, D., 2023. Land subsidence in the Singapore coastal area with long time series of TerraSAR-X SAR data. Remote Sens. 15. https://doi.org/10.3390/rs15092415.
Berardino, P., Fornaro, G., Lanari, R., Sansosti, E., 2002. A new algorithm for surface deformation monitoring based on small baseline differential SAR interferograms. IEEE Trans. Geosci. Remote Sens. 40, 2375–2383. https://doi.org/10.1109/tgrs.2002.803792.
Bo, M.W., Arulrajah, A., Horpibulsuk, S., Leong, M., 2015. Quality management of prefabricated vertical drain materials in mega land reclamation projects: a case study. Soils Found. 55, 895–905. https://doi.org/10.1016/j.sandf.2015.06.019.
Bokhari, R., Shu, H., Tariq, A., Al-Ansari, N., Guluzade, R., Chen, T., Jamil, A., Aslam, M., 2023. Land subsidence analysis using synthetic aperture radar data. Heliyon 9, e14690. https://doi.org/10.1016/j.heliyon.2023.e14690.
Ciampalini, A., Solari, L., Giannecchini, R., Galanti, Y., Moretti, S., 2019. Evaluation of subsidence induced by long-lasting buildings load using InSAR technique and geotechnical data: the case study of a freight terminal (Tuscany, Italy). Int. J. Appl. Earth Obs. Geoinf. 82. https://doi.org/10.1016/j.jag.2019.101925.
Duo, L., Hu, Z., Yang, K., Li, Y., 2022. Sediment settlement rate and consolidation time of filling reclamation in coal mining subsidence land. Int. J. Coal Sci. Technol. 9. https://doi.org/10.1007/s40789-022-00508-x.
Ebmeier, S.K., 2016. Application of independent component analysis to multitemporal InSAR data with volcanic case studies. J. Geophys. Res. Solid Earth 121, 8970–8986. https://doi.org/10.1002/2016jb013765.
Erten, E., Rossi, C., 2019. The worsening impacts of land reclamation assessed with Sentinel-1: the Rize (Turkey) test case. Int. J. Appl. Earth Obs. Geoinf. 74, 57–64. https://doi.org/10.1016/j.jag.2018.08.007.
Feng, T., Xu, N., 2021. Satellite-based monitoring of annual coastal reclamation in Shenzhen and Hong Kong since the 21st century: a comparative study. J. Marine Sci. Eng. 9. https://doi.org/10.3390/jmse9010048.
Ferretti, A., Prati, Claudio, Rocca, Fabio, 2001. Permanent scatterers in SAR interferometry. IEEE Trans. Geosci. Remote Sens. 39 (1), 8–20.
Ferretti, A., Fumagalli, A., Novali, F., Prati, C., Rocca, F., Rucci, A., 2011. A new algorithm for processing interferometric data-stacks: SqueeSAR. IEEE Trans. Geosci. Remote Sens. 49, 3460–3470. https://doi.org/10.1109/tgrs.2011.2124465.
Gaddes, M.E., Hooper, A., Bagnardi, M., Inman, H., Albino, F., 2018. Blind signal separation methods for InSAR: the potential to automatically detect and monitor signals of volcanic deformation. J. Geophys. Res. Solid Earth 123. https://doi.org/10.1029/2018jb016210.
Glaser, R., Haberzettl, P., Walsh, R.P.D., 1991. Land reclamation in Singapore, Hong Kong and Macau. GeoJournal 24, 365–373.
Gualandi, A., Liu, Z., 2021. Variational Bayesian independent component analysis for InSAR displacement time-series with application to Central California, USA. J. Geophys. Res. Solid Earth 126. https://doi.org/10.1029/2020jb020845.
Gualandi, A., Serpelloni, E., Belardinelli, M.E., 2015. Blind source separation problem in GPS time series. J. Geod. 90, 323–341. https://doi.org/10.1007/s00190-015-0875-4.
Henry Cheung, C.H.Y., Cheung, Chris, Wong, Anthony, 2022. Deep Cement Mixing–The Experience in Tung Chung East Reclamation and Challenges Ahead. In: AIJR Proceedings, pp. 348–360. https://doi.org/10.21467/proceedings.133.
Hu, X., Oommen, T., Lu, Z., Wang, T., Kim, J.-W., 2017. Consolidation settlement of salt Lake County tailings impoundment revealed by time-series InSAR observations from multiple radar satellites. Remote Sens. Environ. 202, 199–209. https://doi.org/10.1016/j.rse.2017.05.023.

Huang, R., Ni, P., Yang, W., Chen, Z., Dong, Q., Mei, G., 2023. Semianalytical solution for consolidation of reclaimed land with horizontal drains. Int. J. Geomechan. 23. https://doi.org/10.1061/ijgnai.Gmeng-7921.
Hyvarinen, A., 2013. Independent component analysis: recent advances. Philos. Trans. A Math. Phys. Eng. Sci. 371, 20110534. https://doi.org/10.1098/rsta.2011.0534.
Jiang, L., Lin, H., 2010. Integrated analysis of SAR interferometric and geological data for investigating long-term reclamation settlement of Chek lap Kok airport, Hong Kong. Eng. Geol. 110, 77–92. https://doi.org/10.1016/j.enggeo.2009.11.005.
Jiang, M., Ding, X., Hanssen, R.F., Malhotra, R., Chang, L., 2015. Fast statistically homogeneous pixel selection for covariance matrix estimation for multitemporal InSAR. IEEE Trans. Geosci. Remote Sens. 53, 1213–1224. https://doi.org/10.1109/tgrs.2014.2336237.
Kim, J.S., Kim, D.J., Kim, S.W., Won, J.S., Moon, W.M., 2007. Monitoring of urban land surface subsidence using PSInSAR. Geosci. J. 11, 59–73. https://doi.org/10.1007/bf02910381.
Kravchenko, E., Lu, W., Sauerwein, M., Wong, A.H.K., 2024. Life cycle assessment of waste materials in deep cement mixing for land reclamation in Hong Kong. Environ. Impact Assess. Rev. 105. https://doi.org/10.1016/j.eiar.2023.107398.
Kwong, J.S.M., 1997. A Review of some Drained Reclamation Works in Hong Kong. Geotechnical Engineering Office, Civil Engineering Department.
Lenk, P., 2009. Modelling of primary consolidation. Slovak J. Civil Eng. 17 (2), 26–37.
Liao, M., Zhang, R., Lv, J., Yu, B., Pang, J., Li, R., Xiang, W., Tao, W., 2021. Subsidence monitoring of fill area in Yan'an New District based on sentinel-1A time series imagery. Remote Sens. 13. https://doi.org/10.3390/rs13153044.
Lovisa, J., Read, W., Sivakugan, N., 2011. A critical reappraisal of the average degree of consolidation. Geotech. Geol. Eng. 29, 873–879. https://doi.org/10.1007/s10706-011-9424-y.
Ma, P., Jiang, X., 2024. Mapping vertical and horizonal deformation of the newly reclaimed third runway at Hong Kong international airport with PAZ, COSMO-SkyMed, and Sentinel-1 SAR images. Int. J. Appl. Earth Obs. Geoinf. 132. https://doi.org/10.1016/j.jag.2024.104030.
Ma, P., Wu, Z., Zhang, Z., Au, F.T.K., 2024. SAR-transformer-based decomposition and geophysical interpretation of InSAR time-series deformations for the Hong Kong-Zhuhai-Macao bridge. Remote Sens. Environ. 302. https://doi.org/10.1016/j.rse.2023.113962.
Mario Martín-Antón, V.N., María, José, del Campo, José, Santos López-Gutiérrez, M., Esteban, Dolores, 2016. Review of coastal land reclamation situation in the world. J. Coast. Res. 75, 667–671.
Maubant, L., Pathier, E., Daout, S., Radiguet, M., Doin, M.P., Kazachkina, E., Kostoglodov, V., Cotte, N., Walpersdorf, A., 2020. Independent component analysis and parametric approach for source separation in InSAR time series at regional scale: application to the 2017–2018 slow slip event in Guerrero (Mexico). J. Geophys. Res. Solid Earth 125. https://doi.org/10.1029/2019jb018187.
Mesri, G., Feng, T.W., 2014. Consolidation of Soils. From Soil Behavior Fundamentals to Innovations in Geotechnical Engineering: Honoring Roy E. Olson, pp. 322–337.
Ng, M.K., 2018. Transformative urbanism and reproblematising land scarcity in Hong Kong. Urban Stud. 57, 1452–1468. https://doi.org/10.1177/0042098018800399.
Oja, E., Yuan, Z., 2006. The fastICA algorithm revisited: convergence analysis. IEEE Trans. Neural Netw. 17, 1370–1381. https://doi.org/10.1109/TNN.2006.880980.
Osmanoğlu, B., Sunar, F., Wdowinski, S., Cabral-Cano, E., 2016. Time series analysis of InSAR data: methods and trends. ISPRS J. Photogramm. Remote Sens. 115, 90–102. https://doi.org/10.1016/j.isprsjprs.2015.10.003.
Park, S.W., Hong, S.H., 2021. Nonlinear modeling of subsidence from a decade of InSAR time series. Geophys. Res. Lett. 48. https://doi.org/10.1029/2020gl090970.
Pati, R., Pujari, A.K., Gahan, P., Kumar, V., 2021. Independent component analysis: a review, with emphasis on commonly used algorithms and contrast function. Computación y Sistemas 25. https://doi.org/10.13053/cys-25-1-3449.
Peng, M., Lu, Z., Zhao, C., Motagh, M., Bai, L., Conway, B.D., Chen, H., 2022. Mapping land subsidence and aquifer system properties of the Willcox Basin, Arizona, from InSAR observations and independent component analysis. Remote Sens. Environ. 271. https://doi.org/10.1016/j.rse.2022.112894.
Pickles, A.R., R.T, 1998. Settlement of reclaimed land for the new Hong Kong international airport. Proceed. Institut. Civil Eng.-Geotechn. Eng. 131, 191–209.
Radhika, B.P., Krishnamoorthy, A., Rao, A.U., 2017. A review on consolidation theories and its application. Int. J. Geotech. Eng. 14, 9–15. https://doi.org/10.1080/19386362.2017.1390899.
Sakleshpur, V.A., Prezzi, M., Salgado, R., 2018. Ground engineering using prefabricated vertical drains: a review. Geotech. Eng. J. SEAGS & AGSSEA 49, 45–64.
Shafiee, A., 2008. Permeability of compacted granule–clay mixtures. Eng. Geol. 97, 199–208. https://doi.org/10.1016/j.enggeo.2008.01.002.
Shen, H., Li, X., Duan, R., Zhao, Y., Zhao, J., Che, H., Liu, G., Xue, Z., Yan, C., Liu, J., Jiang, C., Li, B., Chang, H., Gao, J., Yan, Y., 2023. Quality evaluation of ground improvement by deep cement mixing piles via ground-penetrating radar. Nat. Commun. 14, 3448. https://doi.org/10.1038/s41467-023-39236-4.
Shi, G., Lin, H., Ma, P., 2018. A hybrid method for stability monitoring in low-coherence urban regions using persistent and distributed Scatterers. IEEE J. Select. Top. Appl. Earth Observat. Remote Sens. 11, 3811–3821. https://doi.org/10.1109/jstars.2018.2867832.
Shi, G., Lin, H., Bürgmann, R., Ma, P., Wang, J., Liu, Y., 2019. Early soil consolidation from magnetic extensometers and full resolution SAR interferometry over highly decorrelated reclaimed lands. Remote Sens. Environ. 231. https://doi.org/10.1016/j.rse.2019.111231.
Shi, G., Ma, P., Lin, H., Huang, B., Zhang, B., Liu, Y., 2020. Potential of using phase correlation in distributed Scatterer InSAR applied to built scenarios. Remote Sens. 12. https://doi.org/10.3390/rs12040686.
Shi, G., Huang, B., Leung, A.K., Ng, C.W.W., Wu, Z., Lin, H., 2022a. Millimeter slope ratcheting from multitemporal SAR interferometry with a correction of coastal tropospheric delay: a case study in Hong Kong. Remote Sens. Environ. 280. https://doi.org/10.1016/j.rse.2022.113148.
Shi, X., Chen, C., Dai, K., Deng, J., Wen, N., Yin, Y., Dong, X., 2022b. Monitoring and predicting the subsidence of Dalian Jinzhou Bay international airport, China by integrating InSAR observation and Terzaghi consolidation theory. Remote Sens. 14. https://doi.org/10.3390/rs14102332.
Shukla, S., Sivakugan, N., Das, B., 2013. Methods for determination of the coefficient of consolidation and field observations of time rate of settlement — an overview. Int. J. Geotech. Eng. 3, 89–108. https://doi.org/10.3328/ijge.2009.03.01.89-108.
Strozzi, T., Wegmuller, U., Werner, C.L., Wiesmann, A., Spreckels, V., 2003. JERS SAR interferometry for land subsidence monitoring. IEEE Trans. Geosci. Remote Sens. 41, 1702–1708. https://doi.org/10.1109/tgrs.2003.813273.
Sun, Q., Jiang, L., Jiang, M., Lin, H., Ma, P., Wang, H., 2018. Monitoring coastal reclamation subsidence in Hong Kong with distributed Scatterer interferometry. Remote Sens. 10. https://doi.org/10.3390/rs10111738.
Tabish, R., Yang, Z., Wu, L., Xu, Z., Cao, Z., Zheng, K., Zhang, Y., 2022. Predicting the settlement of mine waste dump using multi-source remote sensing and a secondary consolidation model. Front. Environ. Sci. 10. https://doi.org/10.3389/fenvs.2022.885346.
Tazlo Strozzi, U.W., Tosl, Luigl, Bitelli, Gabrlele, Spreckels, Volker, 2001. Land subsidence monitoring with differential SAR interferometry. Photogramm. Eng. Remote. Sens. 67 (11).
Teatini, P., Tosi, L., Strozzi, T., Carbognin, L., Wegmuller, U., Rizzetto, F., 2005. Mapping regional land displacements in the Venice coastland by an integrated monitoring system. Remote Sens. Environ. 98, 403–413. https://doi.org/10.1016/j.rse.2005.08.002.
Tewatia, S.K., 2012. Trend of settlement in primary and secondary consolidations. Geomech. Geoeng. 8, 125–134. https://doi.org/10.1080/17486025.2012.698023.
Tewatia, S.K., Sridharan, A., Singh, M., Rath, S., 2011. Theoretical equations of vertical and radial consolidation by equating degrees of consolidation by settlement analysis and dissipation of pore pressure. Geotech. Geol. Eng. 30, 1037–1043. https://doi.org/10.1007/s10706-011-9485-y.
Tharwat, A., 2020. Independent component analysis: an introduction. Appl. Comput. Informat. 17, 222–249. https://doi.org/10.1016/j.aci.2018.08.006.
Voottipruex, P., Bergado, D.T., Suksawat, T., Jamsawang, P., Cheang, W., 2011. Behavior and simulation of deep cement mixing (DCM) and stiffened deep cement mixing (SDCM) piles under full scale loading. Soils Found. 51, 307–320. https://doi.org/10.3208/sandf.51.307.
Waheed, M., Asmael, N., 2023. Study immediate and consolidation settlement of shallow foundations. Civil Environ. Eng. 19, 318–327. https://doi.org/10.2478/cee-2023-0028.
Wahls, H.E., 1962. Analysis of primary and secondary consolidation. J. Soil Mechan. Foundat. Division 88 (6), 207–231.
Werner, C., Wegmuller, U., Strozzi, T., Wiesmann, A., 2003. Interferometric point target analysis for deformation mapping. IGARSS 2003. In: 2003 IEEE International Geoscience and Remote Sensing Symposium. IEEE, pp. 4362–4364.
Wu, J., Shi, X., Xue, Y., Zhang, Y., Wei, Z., Yu, J., 2007. The development and control of the land subsidence in the Yangtze Delta, China. Environ. Geol. 55, 1725–1735. https://doi.org/10.1007/s00254-007-1123-x.
Wu, S., Yang, Z., Ding, X., Zhang, B., Zhang, L., Lu, Z., 2020. Two decades of settlement of Hong Kong international airport measured with multi-temporal InSAR. Remote Sens. Environ. 248. https://doi.org/10.1016/j.rse.2020.111976.
Xiao, R., Jiang, M., Li, Z., He, X., 2022. New insights into the 2020 Sardoba dam failure in Uzbekistan from earth observation. Int. J. Appl. Earth Obs. Geoinf. 107. https://doi.org/10.1016/j.jag.2022.102705.
Yang, M., Yang, T., Zhang, L., Lin, J., Qin, X., Liao, M., 2018. Spatio-temporal characterization of a reclamation settlement in the Shanghai coastal area with time series analyses of X-, C-, and L-band SAR datasets. Remote Sens. 10. https://doi.org/10.3390/rs10020329.
Yu, Q., Wang, Q., Yan, X., Yang, T., Song, S., Yao, M., Zhou, K., Huang, X., 2020. Ground deformation of the Chongming east shoal reclamation area in Shanghai based on SBAS-InSAR and laboratory tests. Remote Sens. 12. https://doi.org/10.3390/rs12061016.
Yu, Q., Yan, X., Wang, Q., Yang, T., Lu, W., Yao, M., Dong, J., Zhan, J., Huang, X., Niu, C., Zhou, K., 2021. A spatial-scale evaluation of soil consolidation concerning land subsidence and integrated mechanism analysis at macro-, and Micro-scale: a case study in Chongming east shoal reclamation area, Shanghai, China. Remote Sens. 13. https://doi.org/10.3390/rs13122418.
Zeng, L.L., Hong, Z.S., Cui, Y.J., 2015. On the volumetric strain–time curve patterns of dredged clays during primary consolidation. Géotechnique 1-6. https://doi.org/10.1680/geot.15.T.003.
Zhang, X., Li, M., Sun, Y., Zhu, Y., Yang, Z., Tian, D., 2019. Study on permeability coefficient of saturated cohesive soil based on fractal theory. In: IOP Conference Series: Earth and Environmental Science, 242, p. 062055.
Zhao, Q., Lin, H., Gao, W., Zebker, H.A., Chen, A., Yeung, K., 2011. InSAR detection of residual settlement of an ocean reclamation engineering project: a case study of Hong Kong international airport. J. Oceanogr. 67, 415–426. https://doi.org/10.1007/s10872-011-0034-3.
Zhao, Q., Ma, G., Wang, Q., Yang, T., Liu, M., Gao, W., Falabella, F., Mastro, P., Pepe, A., 2019. Generation of long-term InSAR ground displacement time-series through a novel multi-sensor data merging technique: the case study of the Shanghai coastal area. ISPRS J. Photogramm. Remote Sens. 154, 10–27. https://doi.org/10.1016/j.isprsjprs.2019.05.005.